Universidad de Concepción
Facultad de Ciencias Físicas y Matemáticas

Life of a Hero –
Hercules, Stream or Dwarf Galaxy?

Tesis que presenta

Matías Andrés Blaña Díaz

Para optar al título profesional de Astrónomo que otorga la Carrera Ciencias Físicas y Astronómicas

Profesor Guía: Dr. Michael Fellhauer

Departamento de Astronomía
Departamento de Física
Facultad de Ciencias Físicas y Matemáticas
Universidad de Concepción

Concepción, Chile
5 de Diciembre del 2012

Life of a Hero - Hercules, Stream or Dwarf Spheroidal Galaxy?

Student: *Matias Andrés Blaña Díaz*[1,2] [*]

Evaluating committee:

Advising Professor *Dr. Michael Fellhauer*[2] [†]

Professor *Dr. Ricardo Demarco* [2] [‡]

and

Professor *Dr. Neil Nagar*[2] [§]

[1] Departamento de Física, Universidad de Concepción, Concepción, Chile
[2] Departamento de Astronomía, Universidad de Concepción, Concepción, Chile

January 23, 2013

[*]E-mail: mblana@astro-udec.cl
[†]mfellhauer@astro-udec.cl
[‡]rdemarco@astro-udec.cl
[§]nagar@astro-udec.cl

Resumen

La Vía Láctea esta rodeada por numerosas galaxias enanas esferoidales. Se cree que sus propiedades cinemáticas se explican por su posible contenido de materia obscura. Pero en otros casos sus propiedades cinemáticas son explicadas por su disrupción producto de las fuerzas de marea de su galaxia anfitriona, como es el caso de la corriente de Sagitario. La galaxia enana esferoidal Hércules esta a una distancia de 138 kpc del centro de la Vía Láctea y tiene una velocidad radial de $v_{\rm rad}^{\rm GSR} = 144$ km s^{-1} en el Sistema de Referencia Galáctico (GSR). Adén et al. (2009b) calcularon una dispersión de velocidades de $\sigma_{\rm los} = 3.72 \pm 0.91$ km s^{-1} y asumiendo equilibrio virial los autores estiman una masa dinámica de $1.9^{+1.1}_{-0.8} \times 10^6$ M$_\odot$ dentro de un radio de 300 pc, un valor mucho más bajo del esperado para galaxias tan poco luminosas como Hércules. Ellos también calcularon un gradiente de velocidades radiales de $\Delta v_{\rm rad} = 16{\pm}3$ km s^{-1} kpc^{-1} que atribuyen a rotación. Pero su forma elongada sugiere una posible disrupción producto de las fuerzas de marea de la Vía Láctea. Jin & Martin (2010) dedujeron una velocidad tangencial de $v_{\rm tang}^{\rm GSR} = -16^{+6}_{-22}$ km s^{-1} a lo largo de la elongación y determinaron una posible órbita usando argumentos de energía y momento angular. Nosotros reprodujimos esta órbita y también otras en la misma dirección de la elongación para encontrar un modelo para Hércules mediante simulaciones N-Body. No pudimos reproducir la gran elipticidad de Hércules, pero si pudimos reproducir seis parámetros observacionales dentro de sus errores observacionales: el brillo superficial central, la masa luminosa, el radio efectivo, la orientación de la elongación, la dispersión de velocidades central y el gradiente de velocidades radiales. En nuestros modelos la disrupción por fuerzas de marea también puede explicar la velocidad de dispersión medida en Hércules sin la necesidad de materia obscura. También encontramos un área única de soluciones en el espacio de parametros para la masa inicial (M$_{\rm init}$) y para el tamaño inicial (R$_{\rm Plum}$) del progenitor de Hércules, usando una órbita de 10 Gyr: Un R$_{\rm Plum}$ entre 68 pc y 80 pc, y una M$_{\rm init}$ entre $1.6{\times}10^5$ M$_\odot$ y $2.5{\times}10^5$ M$_\odot$, implicando una pérdida de masa de entre 70% y 80%.

Abstract

The Milky Way (MW) is surrounded by several dwarf spheroidal galaxies (dSph). Their kinematical properties are thought to be explainable by their dark matter content. But in other cases the kinematics of dwarf galaxies are explained through the tidal disruption caused by its host galaxy, like in the Sagittarius Stream. The Hercules dSph galaxy is located at a distance of 138 kpc from the MW and it has a radial velocity of $v_{\rm rad}^{\rm GSR} = 144$ km s^{-1} in the Galactic Standard of Rest frame (GSR). Adén et al. (2009b) calculated a velocity dispersion of $\sigma_{\rm los} = 3.72 \pm 0.91$ km s^{-1} and assuming virial equilibrium the authors estimate a dynamical mass of $1.9^{+1.1}_{-0.8} \times 10^6$ $M_\odot$ within radius of 300 pc, a value much lower than the expected for dSph galaxis as faint as Hercules. They also calculated a radial velocity gradient of $\Delta v_{\rm rad} = 16 \pm 3$ km s^{-1} kpc^{-1} and they attributed it to rotation. But, its elongated shape suggests a possible tidal disruption caused by the gravitational force of the Milky Way. Jin & Martin (2010) deduced a tangential velocity of $v_{\rm tang}^{\rm GSR} = -16^{+6}_{-22}$ km s^{-1} along the elongation and determined a possible orbit using energy and angular momentum arguments. We reproduce this orbit and also other orbits in the same direction of the elongation to find a suiteable model for Hercules through N-Body simulations. We cannot reproduce the high ellipticity of Hercules, but we match six other observational parameters within their observational errors: the central surface-brightness, the luminous mass, the effective radius, the orientation of the elongation, the central line-of-sight velocity-dispersion and the gradient of radial velocities. In our models the tidal disruption also could explain the measured velocity-dispersions in Hercules without the need of dark matter. We also find a unique and narrow solution area of the parameter-space for the initial luminous mass ($M_{\rm init}$) and the initial size ($R_{\rm Plum}$) of the progenitor of Hercules using a 10 Gyr orbit: A $R_{\rm Plum}$ between 68 pc and 80 pc, and an $M_{\rm init}$ between 1.6×10^5 $M_\odot$ and 2.5×10^5 $M_\odot$, implying a mass-loss between 70% and 80%.

Contents

1 Introduction

1.1 The Dwarf Spheroidal Galaxies of the Milky Way

Around the Milky Way (MW) more than 20 dwarf galaxies orbiting at distances closer than 250 kpc have been discovered. The dwarf Leo T (Irwin et al., 2007) is an exception, located at a distance of 417 kpc. Most probably there are many others too far or too faint waiting to be discovered. The dwarf galaxies (dG) in the MW are classified in two categories: the dwarf irregular galaxies (dIrr) and the dwarf spheroidal galaxies (dSph). There are only two dwarf Irregulars, the Large Magellanic Cloud (LMC) and the Small Magellanic Cloud (SMC). These two galaxies are the most luminous of the collection of satellites, having about 2.1×10^9 $L_\odot$ for the LMC and 5.7×10^8 $L_\odot$ for the SMC and observations indicate that they still have gas and form stars. The majority of the satellites of the MW are dwarf spheroidal galaxies (dSph). We show the main properties of some of them in Table 1. The first dSphs detected around the MW were the nine Classical dSph galaxies, which have luminosities ranging from 4.5×10^4 $L_\odot$ to 2.0×10^7 $L_\odot$. The last discovered Classical dSph galaxy, Sagittarius, was found by Ibata et al. (1995) showing clear signs of being in the last stages of disruption and dissolution, caused by the tidal effects of the MW. Sagittarius also shows the most prominent tidal tails spanning all across the sky (Belokurov et al., 2006). The number of discovered dSph galaxies increased to more than the double with the arrival of the automated telescope of the Sloan Digital Sky Survey (York et al., 2000) adding many faint and ultra-faint dwarf spheroidal galaxies to the list.

An important characteristic of the dSphs is that they are fainter than some star clusters, having luminosities ranging from $\sim 10^3$ $L_\odot$ to $\sim 10^7$ $L_\odot$ and very low stellar densities, with central fluxes of 30 $L_\odot$ pc^{-2} (for Leo I) or 2.2 $L_\odot$ pc^{-2} (for Draco) (see Irwin et al. (1995)). A second important fact is that most of them show short epochs of star formation with very old stellar populations, as shown in Figure 1 (Grebel E., 2000). Their populations are around 10 Gyr old or even older.

It has been proposed that the dwarfs helped in the creation of the stellar halo of the MW as they became disrupted and formed streams. If this is true, the abundance of chemical elements should be similar. Kirby et al. (2008) found metallicities in the dSph, that are low enough to be comparable with the metallicity found in the stars of the MW's halo. They found mean metallicities of $\langle$[Fe/H]$\rangle \approx -2.7$ to $\langle$[Fe/H]$\rangle \approx -1$, and founding stars even more metal-poor than [Fe/H] $= -3.0$. But there is a problem with the abundances of α-elements and neutron-capture elements. Compared at the same metallicity, the samples of dSph stars have abundance ratios slightly lower than that is measured in the stars of the halo. Franois et al. (2012) show that the same is true for stars of the dSph Hercules. Kirby et al. (2008) also show an interesting correlation for the dSph galaxies, if the luminosity increases then the metallicity increases exponentially.

The most surprising characteristic of the dwarf spheroidals appeared with the measurements of the radial velocities of their stars and the calculation of their velocity-dispersions. In a sample of dSphs, Simon & Geha (2007) deduce central velocity dispersions ranging from 3.3 ± 1.7 km s^{-1} for Leo IV to 7.6 ± 0.4 km s^{-1} for Canes Venatici I. Walker et al. (2007)

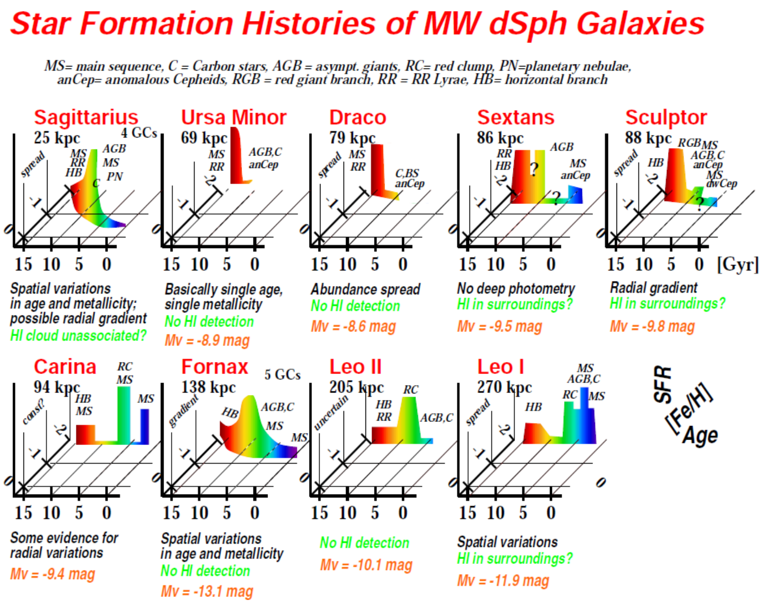

Figure 1: Star formation histories of the dwarf spheroidal galaxies according to Grebel E. (2000). Each population box gives a schematic representation of star formation rate (SFR) as a function of age and metallicity. There is a crude tendency for increased intermediate-age population fractions with increased Galactocentric distance and dwarf galaxy mass.

measured in seven of the Classical dSph how changes the line-of-sight velocity-dispersion profile with the projected radius $[\sigma_{los}(R)]$. They found that the profiles do not decrease like the profile of the surface brightness, but instead the dispersions at the outer parts are as high as in the core. With arguments from stellar dynamics and the assumption of virial equilibrium, which we discuss in Section 2, it is possible to relate the velocity dispersion of the stars with a density profile of the total mass measured dynamically. The resulting dynamical masses are one or two orders of power higher than the luminous mass for each case. Simon & Geha (2007) obtain mass-to-light ratios in Ursa Major I and Leo IV of 1024 ± 636 $M_\odot/L_\odot$ and 151 ± 177 $M_\odot/L_\odot$ respectively. Dwarf galaxies such as the Sagittarius Stream also show high velocity dispersions due to the tidal disruption and not to virial equilibrium. In the following sections we discuss in more detail this two possible explanations for the high velocity dispersions.

1.2 Possible Origins of Dwarf Spheroidal Galaxies

1.2.1 The Dwarf Spheroidal Galaxies and the Dark Matter Subhaloes in the ΛCDM Model

It was already mentioned that, under the assumption of dynamical or virial equilibrium, the velocity-dispersion of the dSph galaxies are too high to be explained by only luminous matter and therefore additional mass is required. Using similar dynamical arguments, the existence

Table 1: Properties of some dSph galaxies taken from (Kroupa et al., 2010), (Walker et al., 2009b), (Adén et al., 2009a) and (Jin & Martin, 2010). The first column corresponds to the luminosity in the V band. The second to the distance to the centre of the MW. The third corresponds to the radial velocity in the Galactic Standard of Rest frame. The fourth column is the half light radius and finally the last column corresponds to the central line-of-sight velocity dispersion.

Object	L_V [$L_\odot$]	$D_{\mathrm{Gal.Cen}}$ [kpc]	v_{GSR} [$\mathrm{km\,s^{-1}}$]	r_{h} [pc]	σ_0^{los} [$\mathrm{km\,s^{-1}}$]
Classical dSph:					
Carina	$2.4 \pm 1.0 \times 10^5$	103	22.5 ± 3	241 ± 23	6.6 ± 1.2
Draco	$2.7 \pm 0.4 \times 10^5$	82	-112.3 ± 2	196 ± 12	9.1 ± 1.2
Fornax	$1.4 \pm 0.4 \times 10^7$	140	-29.2 ± 3	668 ± 34	11.7 ± 0.9
Leo I	$3.4 \pm 1.1 \times 10^6$	256	179.9 ± 2	246 ± 19	9.2 ± 1.4
Leo II	$5.9 \pm 1.8 \times 10^5$	208	17.0 ± 2	151 ± 17	6.6 ± 0.7
Sextans	5.4×10^5	89	76.9 ± 3	682 ± 117	7.9 ± 1.3
Sculptor	2.4×10^6	79	77.9 ± 3	260 ± 39	9.2 ± 1.1
Sagittarius	2×10^7	16	161.1 ± 5	1550 ± 50	11.4 ± 0.7
Some new dSph:					
Hercules	$(2.9 \pm 0.7) \times 10^4$	138	144.7 ± 1.2	230 ± 30	3.7 ± 0.9
Leo IV	$(1.8 \pm 0.8 \times 10^4$	156	10.6 ± 1.4	116 ± 30	3.3 ± 1.7
Leo V	$(1.0 \pm 0.8) \times 10^4$	176	58.5 ± 3.1	42 ± 5	2.4 ± 1.9
Ursa Major I	$(1.4 \pm 0.4) \times 10^4$	105	-6.9 ± 1.4	318 ± 45	11.9 ± 3.5
Ursa Major II	$(3.3 \pm 1.0) \times 10^3$	37	-29.0 ± 1.9	140 ± 25	6.7 ± 1.4
Bootes I	$(2.6 \pm 0.5) \times 10^4$	61	94.4 ± 3.4	242 ± 21	6.5 ± 2.0
Bootes II	$(9.2 \pm 5.4) \times 10^2$	43		51 ± 17	10.5 ± 7.4
Canes Venatici I	$(2.0 \pm 0.3) \times 10^5$	213	64.8 ± 0.6	564 ± 36	7.6 ± 0.4
Canes Venatici II	$(7.5 \pm 3.1) \times 10^3$	155	-97.5 ± 1.2	74 ± 12	4.6 ± 1.0

of dark matter (DM) is inferred in galaxies of all scales.

The existence of dark matter is also inferred from models of the standard cosmology, called Lambda Cold Dark Matter (ΛCDM). This model explains the expansion and structure formation of the Universe. This model requires that the total amount of matter and energy in the Universe is composed of 74% dark energy, 3.6% nonluminous matter such as intergalactic gas, Massive Compact Halo Objects (MACHOs) and neutrinos, just 0.4% luminous matter like stars, gas and radiation and a predominating 22% of dark matter (DM).

The study of structure formation in the Universe at galactic and intergalactic scales is possible with large-scale N-body simulations. Navarro, Frenk & White (1997) (NFW) obtained through simulations the first distribution functions for the dark matter structures, discovering the NFW-profile (see Eq. 1). Their models generate an evolutionary process for the Universe, where the matter assembles in small dark matter haloes, which continuously merge forming new and more massive haloes, a process called hierarchical structure formation. The Millennium Simulation (2005) and the Millennium Simulation II (Boylan-Kolchin et al., 2009) simulate a ΛCDM Universe with a scale of 0.74 Gpc and obtain the *cosmic web* produced by the hierarchical formation process. In this mechanism the dark matter haloes work as cocoons, trapping gas which may then form galaxies in the centre of the DM haloes (DMHs), predicting therefore that every galaxy should be embedded in a dark matter halo. According to this mechanism, reproduced at smaller scales in simulations like The Aquarius Project (Springel et al., 2008) and the Via Lactea II (Diemand et al., 2008) shown in Fig. 2, a galaxy like the Milky Way with an estimated dark matter halo of $\sim 10^{12}$ $M_\odot$ should be surrounded by hundreds of dark matter subhaloes. Recent simulations made by Sawala et al. (2012) indicate that the mass needed in these subhaloes to retain their gas and form stars, should be $\sim 10^9$ $M_\odot$ if they evolve in isolation, and $\sim 5 \times 10^9$ $M_\odot$ or more if they evolve as satellites, orbiting inside a more massive DMH. A galaxy like the Milky Way should still have a few hundred dwarf satellites. This seems to be in disagreement with the known number of dwarfs, a fact often dubbed as *the missing satellite problem* (Simon & Geha, 2007). Recent calculations of the possible incompleteness of our known sample of dwarfs suggest that this discrepancy no longer exists (Koposov et al., 2008; Macciò et al., 2009, 2010).

The haloes of Navarro, Frenk & White (1997) with masses from $\sim 3 \times 10^{11}$ $M_\odot$ to $\sim 3 \times 10^{15}$ $M_\odot$ follow a density profile of the form:

$$\rho(r) = \rho_{crit} \frac{\delta_c}{(r/r_s)\,(1 + r/r_s)^2} \tag{1}$$

where r_s is a scale radius, ρ_{crit} is the critical density and δ_c is the characteristic overdensity of the halo, function of the concentration c. For more details see Navarro, Frenk & White (1997).

$$\delta_c = \frac{200}{3} \frac{c^3}{\ln(1 + c) - c/(1 + c)} \tag{2}$$

While the large N-body simulations favour DM density profiles with central divergent or cuspy density-profiles like the NFW-profile, the observations seem to favour profiles with a convergent or cored density-profile (Merrit et al., 2006), like the more recent Einasto-profile.

Another possibility would be that the dSph galaxies were formed by galactic collisions. These collisions produce debris of old stars and gas formed within the tidal tails. In these tails we often see new stars forming and those new, DM-free objects are called Tidal Dwarf Galaxies.

1.2.2 The Tidal Dwarf Galaxies & the Disc-of-Satellites

The origin and properties of the MWs dSph galaxies are still under debate. Kroupa et al. (2005) proposed that most or all the satellites are in fact remnants of a collision of the MW with another massive galaxy, leaving packets of stars called Tidal Dwarf Galaxies (TDGs). The TDG have been observed in extragalactic collisions between disc galaxies and also have been obtained through simulations. Such objects would have no dark matter, in contrary to

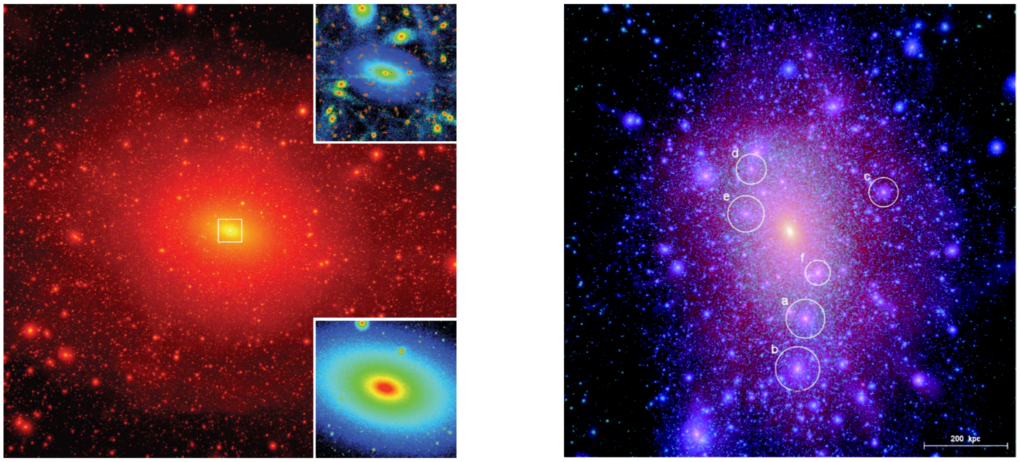

Figure 2: *Left panel*: The Via Lactea II (VLII) simulations, taken from Diemand et al. (2008). We see projected dark matter squared-density map. A cube of 800 kpc per side is shown. The insets focus on an inner cube of 40 kpc per side (outlined in white), and show local density (bottom inset) and local phase-space density calculated with EnBiD (ref. 27; top inset). The VLII simulation has a mass resolution of 4,100M [and a force resolution of 40 pc. The mass within $r_{200} = 402$ kpc of the centre (the radius enclosing 200 times the mean matter density) is $1.931012 M_{\odot}$. *Right panel*: The Aquarius simulation taken from Springel et al. (2008). We see a dark matter distribution in a cubic region of side $2.5 \times r_{50}$ centred on the main halo in the Aq-A-1 simulation. The figure also shows the substructures within the more massive DM halo, showing with marking circles six DM subhaloes (a – f), which also have substructures.

the dSph galaxies in the ΛCDM scenario. In the TDG scenario the high velocity dispersions are due to the tidal disruption of the TDG. As proof Kroupa et al. (2005) claim that all dSph galaxies are located in a disc-like configuration called Disc-of-Satellites (DoS), a plane marking the former plane of the interaction (see Fig. 3 made by Metz et al. (2009)).

1.3 The Hercules Dwarf Spheroidal Galaxy

The Hercules dSph galaxy was discovered recently by Belokurov et al. (2007). Its central surface-brightness is $\mu_0 \sim 27$ mag arcsec^{-2}. We show other important properties of Hercules in Table 2. Hercules lies at a distance of ~ 138 kpc from the Milky Way (Adén et al. (2009a), Sand et al. (2009)) and its luminosity is 2.68×10^4 L$_{\odot}$ (Sand et al., 2009) or 3.87×10^4 L$_{\odot}$ (Coleman et al., 2007). Depending on the chosen stellar mass-to-light ratio, its stellar mass is in the range of the $\sim 5 \times 10^4$ M$_{\odot}$. Like the rest of the dSph galaxies Hercules contains no gas and presents no recent star formation. Adén et al. (2011) study the chemical abundances of [Fe/H], [Ca/H] and a trend in the [Ca/Fe] abundance, which suggests an early rapid chemical enrichment through supernovae of type II, followed by a phase of slow star formation dominated by enrichment through supernovae of type Ia. A comparison with the isochrones indicates that the red giants in Hercules are older than 10 Gyr, which could give us some hints

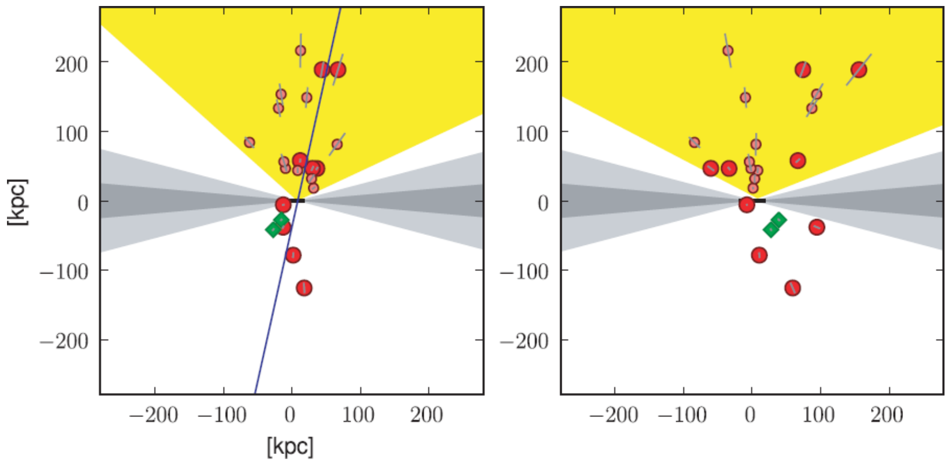

Figure 3: Taken from Metz et al. (2009); The 3D distribution of the MW satellite galaxies. Left panel: an edge-on view on to the fitted Disc-of-Satellites (DoS) as given in Metz et al. (2007) is shown. The MW disc, located in the centre of the plot, is seen edge-on. Right panel: a view rotated by $90^{\rm o}$ about the polar axis of the MW is shown. The Magellanic Clouds are marked by diamond symbols, the dwarf spheroidals by circles, where as the smaller circles mark the newly discovered satellites (Table 1). Uncertainties are indicated by light grey bars. In addition, the obscuration region, $|b| < 5^{\rm o}$, of the MW is shown as the dark-shaded region (the light-shaded region being the $15^{\rm o}$ obscuration region). The projected northern sky coverage region of the SDSS is indicated by the yellow-coloured area.

about the age of this object. The elongated structure observed in Hercules by Coleman et al. (2007) using the Large Binocular Telescope (LBT) (see Fig. 4) suggests that it may be in the process of tidal disruption. Adén et al. (2009a) determine a line-of-sight velocity dispersion of $\sigma_{\rm los}$ = 3.72±0.91 km s^{-1}, and also a radial velocity gradient of -16±3 km s^{-1} kpc^{-1}. From this the authors induce that Hercules has a component of stars orbiting in rotation. We show the spatial distribution of some star-members and the radial velocity gradient in Fig. 5. This gradient could also be associated with an effect of tidal distortion caused by the Milky Way instead of rotation. Assuming that Hercules is in tidal disruption, Jin & Martin (2010) proposed an orbit. Using the measured radial velocities of the stars of Hercules and the orientation of the elongation of Hercules, the authors estimate a tangential velocity using energy and angular momentum arguments.

Sand et al. (2009) estimate a projected half-light radius of $r_h = 230 \pm 30$ pc and a projected ellipticity of $\epsilon = 0.67 \pm 0.03$. And with the assumptions of Jin & Martin (2010) a deprojected half-light radius and ellipticity of $r_{h,deproj} = 1.5$ kpc and $\epsilon_{deproj} = 0.95$ are estimated.

Table 2: Observational properties of Hercules. (Adén et al. (2009a) and Jin & Martin (2010).

Parameter	Value
RA (J2000)	$16^{\rm h}\ 31^{\rm m}\ 02\overset{\rm s}{.}0 \pm 14$”
Dec (J2000)	$12^{\rm o}\ 47^{\rm m}\ 13\overset{\rm s}{.}83 \pm 5$”
Dist	138 ± 7 [kpc]
E(B-V)	0.055 ± 0.005 (mag)
$(\text{m-M})_0$	20.6 ± 0.2 (mag)
$\bar{v}_{\rm GSR}$	144.7 ± 1.2 [km s^{-1}]
$\text{L}_{\rm V}$	$3.6 \pm 1.1 \times 10^4$ [$\text{L}_\odot$]
$\text{M}_{\rm V}$	-6.6 ± 0.3
$\mu_{0,\rm V}$	27.2 ± 0.6 [$mag/arcsec^2$]
$\text{M}_{Stellar}$	$5 \pm 1.5 \times 10^4$ [$M_\odot$]
r_{half}	230 ± 30 [pc]
$[Fe/H]$	-2.1 ± 0.2

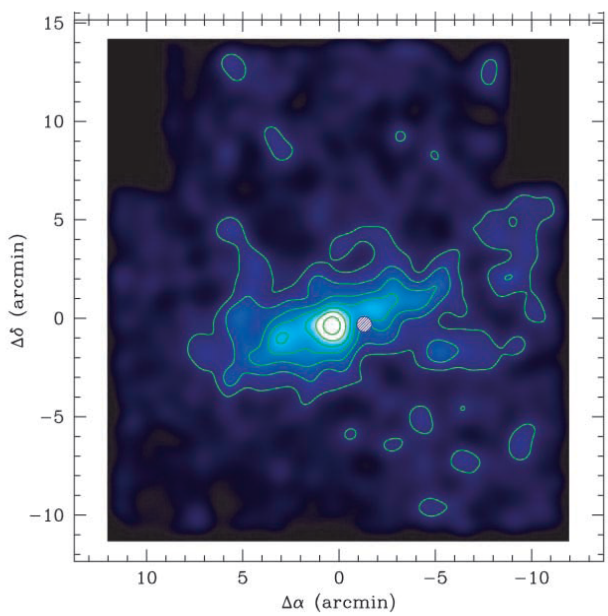

Figure 4: Contour diagram taken from Coleman et al. (2007), made using the CMD-selected sources by the authors. Each star has been convolved with a Gaussian of width 0.6 arcmin. The contours correspond to stellar densities of 1.5σ, 3σ,...,10.5σ above the background stellar density from Poisson statistics. At a distance to Hercules of 138 kpc, 10 arcmin corresponds to approximately 400 pc.

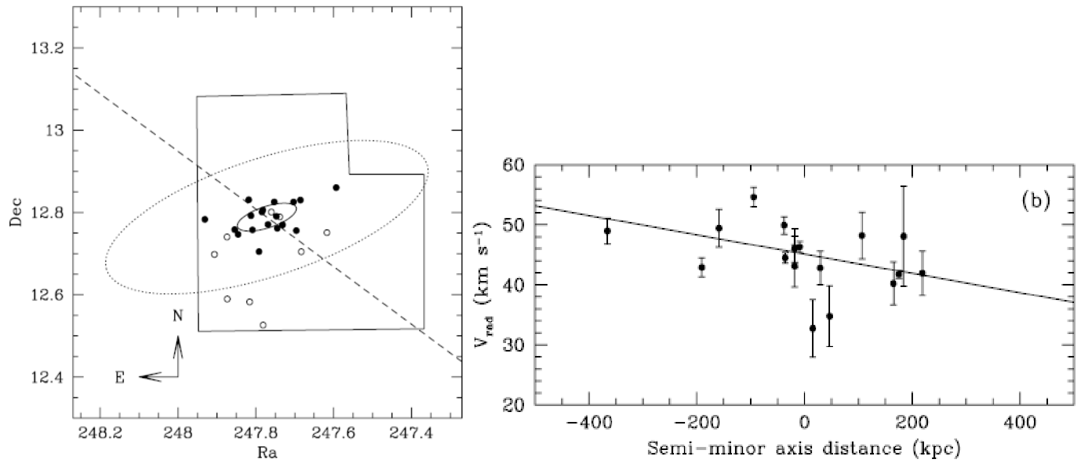

Figure 5: Taken from Adén et al. (2009b). *Left*: The spatial distribution on the sky of stars identified as Hercules members. The dashed line indicates the semi-minor axis for the position angle of the rotation axis that the authors claim. *Right*: The radial velocity distribution of the stars versus the semi-minor axis distance, where the slope reveals a radial velocity gradient.

2 Stellar Dynamics

Dwarf spheroidal galaxies are objects with long relaxation times (longer than the age of the universe) and are devoid of gas. These facts allow us to model these objects as pure stellar dynamical entities using collision-less N-body codes without the need to include hydrodynamics (Binney & Tremaine, 2008).

2.1 Equilibrium and the Dynamical Mass

If we assume that the dSph galaxies are in virial equilibrium, i.e. they are in a stable and unchanging configuration, they have a fixed ratio between their total kinetic (K) and total potential (W) energies:

$$W = -2K \tag{3}$$

We can relate the velocity dispersion of 'pressure' supported systems (σ) and their scale-length ($\mathrm{r_h}$) with a mass-estimate required to keep the system in a stable and unchanging configuration. We call this dynamically calculated mass 'dynamical mass' ($\mathrm{M_{dyn}}$); (Binney & Tremaine, 2008):

$$\sigma^2 = 0.4\frac{GM_{\mathrm{dyn}}}{r_{\mathrm{h}}} \tag{4}$$

Assuming the objects follow a lowered isothermal distribution like a King profile we can rewrite Eq.4 in the following form (Illingworth, 1976):

$$M_{\mathrm{dyn}} = 167 r_{\mathrm{core}} \sigma_0^2 \tag{5}$$

where r_{core} is the core radius of the King profile and σ_0 is the central velocity dispersion.

The dSph galaxies are very low-luminosity objects, i.e. their mass in stars is very low. But their stars exhibit high velocity-dispersions. Therefore, if these galaxies really are in dynamical equilibrium, they have to be dark matter dominated objects, with mass-to-light ratios from dozens to thousands.

Another way to deduce the mass from the dynamics of the dwarf is via the Jeans equations (Binney & Tremaine, 2008, Eq. 4.19).

Adén et al. (2009b) do an analytical analysis of Hercules considering that it is in dynamical equilibrium, spherically symmetric, has an isotropic velocity-distribution and a flat velocity-dispersion profile. With these assumptions they reduce the Jeans equations to the form:

$$\sigma_v^2 \frac{d\rho\,(r)}{dr} = -\frac{\rho\,(r)\,G\,M\,(r)}{r^2} \tag{6}$$

They fit a deprojected Sérsic density-profile $\rho(r) = \rho_0 (r/\alpha)^{-0.445} e^{-r/\alpha}$ (Klimentowski et al., 2007), to obtain an equation for the mass (M) which depends on the radius (r), and on two parameters, the velocity-dispersion σ_v and the exponential scale radius α, related to the half light radius as $r_h = 1.68\alpha$:

$$M(r) = \frac{r\,(r + 0.445\alpha)\,\sigma_v^2}{\alpha G} \tag{7}$$

They obtain, within a radius of $r = 300$ pc a dynamical mass of $M_{300} = 1.9^{+1.1}_{-0.8} \times 10^6$ M$_\odot$, and within a radius of $r = 433$ pc a dynamical mass of $M_{433} = 3.7^{+2.2}_{-1.6} \times 10^6$ M$_\odot$. Assuming a luminosity of $L = 3.6 \pm 1.1 \times 10^4$ L$_\odot$ (Martin et al., 2008), they find a median mass-to-light ratio of $M_{433}/L = 103^{+83}_{-48} \left[\frac{M_\odot}{L_\odot}\right]$.

2.2 Tidal Effects

When dSph galaxies orbit around a host galaxy like the Milky Way, they feel the tidal (gravitational) forces of their host, which tries to disrupt and transform them into a stream of stars. Depending on the size, mass and trajectory of the dwarf galaxy, their structure may be partially or entirely destroyed. The remaining structure may form a stream with a core of stars that are still gravitationally bound. Examples of the latter are the dwarf galaxies Sagittarius and Canis Major (or Monoceros Ring), which are victims of *the galactic cannibalism* of the Milky Way.

The tidal radius is the distance from the satellite's nucleus at which the gravitational force of the satellite gets canceled by the force of the host galaxy, and the stars further away can no longer be bound to the dwarf galaxy. An analytical approximation of the tidal radius of a satellite is given by the formula of Binney & Tremaine (2008):

$$\mathrm{r_{tidal}} \approx \left(\frac{\mathrm{m_{sat}}}{\mathrm{3M(D)}}\right)^{1/3} \cdot \mathrm{D} \tag{8}$$

This formula relates the mass of the host galaxy M(D) (in our case the MW) within a radius D (the actual distance between the MW and Hercules) with the mass of the satellite $\mathrm{m_{sat}}$ (Hercules). In Tab. 3 we show the change of the size of the tidal radius ($\mathrm{r^D_{tidal}}$) depending on the mass of Hercules at a distance of D=138 kpc. A distance of 138 kpc is too far for significant tidal effects, however, using a velocity and position for Hercules, it is possible to estimate an orbit around the Milky Way, with the assumption of course, of an appropriate potential for the Milky Way.

We calculate the pericentre ($\mathrm{R_{peri}}$) of the orbit proposed by Jin & Martin (2010) from which we can estimate the tidal radius at D=$\mathrm{R_{peri}}$. This new tadial radius is much smaller than that obtained when D=138 kpc (see again Tab. 3 to compare), making the passages through the pericentre extremely traumatic for Hercules due the strong tidal forces of the MW. Therefore, the tidal radius varies significantly depending on how small the pericentre of the orbit is, which can vary between R_{peri}=1.8 kpc and 11.8 kpc (see Tab. 6).

Table 3: Tidal radius ($r^{D}_{\rm tidal}$) of the satellite versus its mass ($m_{\rm sat}$) at distances of D=138 kpc and D=$R_{\rm peri}$=5.7 kpc.

m_{sat}	[$M_\odot$]	10^4	10^5	10^6	10^7	10^8	10^9
$r_{\rm tidal}^{\rm D=138kpc}$	[kpc]	0.23	0.50	1.08	5.03	10.83	23.33
$r_{\rm tidal}^{\rm D=R_{peri}}$	[kpc]	0.02	0.05	0.10	0.46	1.00	2.14

3 The SUPERBOX Code

SUPERBOX is a program that simulates collisionless systems. Therefore it is an ideal tool for simulations of galaxies. This code is based on the particle-mesh (PM) technique, to simulate systems with a high number of particles, up to millions of particles in a reasonable amount of time. The CPU-time (t_{CPU}) scales linearly with the number of particles (N_p), contrary to direct-summation N-body methods, that scales geometrically ($t_{CPU} \sim N_p^2$). Furthermore, the particles in a PM code represent phase-space elements rather than actual stars. The particle number is a way to increase the resolution, but does not reflect the number of stars in the simulated system. In this study we keep the number of particles constant at 10^6, to ensure high resolution, independent of the mass of our models for Hercules. SUPERBOX has high-resolution subgrids following the simulated object (an over-density of particles for example). Pure PM codes neglect collisions or close encounters between particles.

The code uses the density and a stationary Green's function to calculate the gravitational potential by solving the Poisson equation (9) in Fourier space doing a Fast Fourier Transformation (FFT).

$$\nabla^2 \Phi \quad = 4\pi G \rho \tag{9}$$

The potential is used to calculate the accelerations for the particles in each cell. We show the flow-chart for SUPERBOX in Figure 6.

For each galaxy, five grids with 3 different resolutions are used. This is possible by using the additivity of the potential. The grids are display in Figure 6. The five grids are arranged as follow:

1. Grid 1 is the high-resolution grid which resolves the centre of the galaxy. It has a length of $2 \times R_{core}$ in one dimension. In evaluating the densities, all particles of the galaxy within $r \leq 2 \times R_{core}$ are stored in this grid.

2. Grid 2 has an intermediate resolution to resolve the galaxy as a whole. The length is $2 \times R_{out}$, but only particles with $r \leq R_{core}$ are stored here, i.e. the same particles as in grid 1.

3. Grid 3 has the same size and resolution as grid 2, but it only contains particles with $R_{core} < r \leq R_{out}$.

4. Grid 4 has the size of the whole simulation area (i.e. 'local universe' with $2 \times R_{system}$), and has the lowest resolution. It is fixed. Only particles of the galaxy with $r \leq R_{out}$ are stored in grid 4.

5. Grid 5 has the same size and resolution as grid 4. This grid treats the escaping particles of a galaxy, and contains all particles with $r > R_{out}$.

Grids 1 to 3 are focused on a common centre of the galaxy and move with it through the "local universe". All grids have the same number of cells per dimension, N, for all

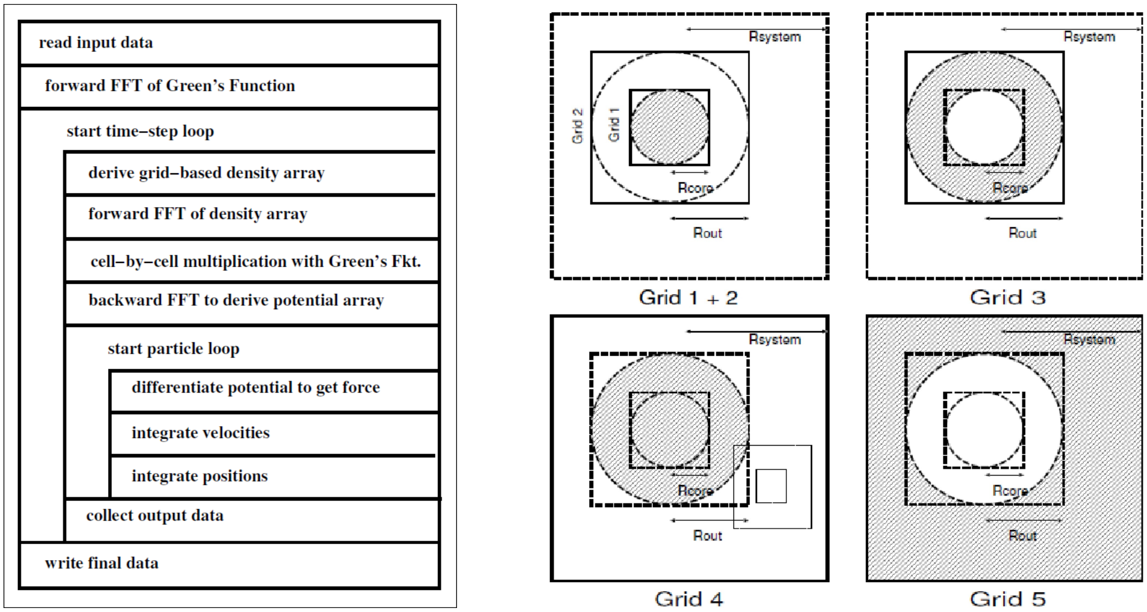

Figure 6: *Left*: Flow-chart for SUPERBOX . *Right*: The five grids of SUPERBOX. In each sub-panel, solid lines highlight the particular grid. Particles are counted in the shaded areas of the grids. The lengths of the arrows are (N/2)-2 grid-cells. In the bottom left sub-panel, the grids of a hypothetical second galaxy are also shown as solid lines. Both figures are taken from Fellhauer et al. (2000).

galaxies. The boundary condition, requiring two empty cells with $\rho = 0$, is open and non-periodic, thus providing an isolated system. This however means that only N-4 active cells per dimension are used.

4 Setup of the Simulations

Our basic procedure consists in using the initial position and velocity of Hercules given by Jin & Martin (2010) to calculate the orbit backwards in time with a simple particle integrator and obtain the position and velocity then. We then use this new position and velocity for our model of Hercules (a Plummer sphere) and let it orbit forward until the present using an N-body code. We change in each simulation the initial mass and initial size of the Plummer sphere to match 7 observational parameters in Hercules. The details are explain now:

4.1 Possible Orbits

We have five main parameters in our models:

1. two sets for the analytical potential of the MW (set i and set ii explained later)
2. the magnitude and direction of the actual tangential velocity v_t of Hercules
3. the total initial mass $M_{\rm tot}^{init} = M_{\rm Plum}$ of our model for Hercules
4. the Plummer radius $R_{\rm Plum}$ of the model
5. the infall time $t_{\rm init}$ of the orbit

4.1.1 Infall Time

dSph galaxies are thought to be the oldest galaxies in the universe, forming before or shortly after reionization (Koposov et al., 2008). As long as they evolve in isolation we do not expect a change in their internal structural parameters. This changes when they start to orbit in the tidal field of the MW. Even in the case where Hercules is a TDG formed in a major merger event of the MW, we would expect such events in the early years of the MW. Therefore our simulation time of 10 Gyr is, even though arbitrary, a good guess. Nonetheless, we also explore infall times of 2 and 5 Gyrs.

4.1.2 Initial Conditions

The position and radial velocity of Hercules are determined by observations, and Jin & Martin (2010) estimated a tangential velocity for Hercules. Following their findings we now have the full phase-space position of Hercules today. We show the proposed velocities of Hercules in rectangular coordinates in Tab. 4.

We now have to assume a suitable potential for the Milky Way to calculate an orbit. Again we follow Jin & Martin (2010) and use their superposition of several analytical potentials to simulate the different structures of the Milky Way (set i). We also analyzed some cases with the standard potential for the MW (set ii). Using sets i) and ii) for the potentials (explained later) we calculate the new positions and velocities of Hercules backwards in time using a simple-particle integration. This new positions and velocities are the initial conditions for our N-body simulations, which are showed in Tab. 5.

We now consider 7 main scenarios or *cases* in our simulations (set i and set ii for the potential of the MW are explained later):

- A This case use the orbit proposed by Jin & Martin (2010): set i for the potential of the MW and a final tangential velocity for Hercules $v_t = -16\ \mathrm{km\,s^{-1}}$, and an infall time of 10 Gyr.
- B This case is the same as case A, but with $v_t = +16\ \mathrm{km\,s^{-1}}$.
- C Same as case A, but with v_t=+38 $\mathrm{km\,s^{-1}}$.
- D Same as A, but with v_t=+10 $\mathrm{km\,s^{-1}}$.
- E Same as B, but with an infall time of: t_{inf} = 2.6 Gyr.
- F Same as B, but with an infall time of: t_{inf} = 5 Gyr.
- G Same as B, but we use set ii) for the potential of the MW.

For each Case we fix 3 parameters: the potential of the MW, the infall time, and the final tangential velocity of Hercules. And we vary the total initial mass M_{tot}^{init} of the Plummer sphere and the Plummer radius, R_{Plum}, trying to match 7 observational quantities: the final luminous mass, the surface-brightness, the effective radius, the angle of inclination, the velocity-dispersion and the velocity-gradient. We then plot for each of the 7 cases (A through G), the initial total mass versus these quantities. For case A we repeat the procedure leaving the initial mass fixed and varying the Plummer radius versus the observed quantities.

Our different sets for the initial conditions give us different orbits, with a range of pericentres that go from R_{per}=1.8 to 11.8 kpc, showed in Tab. 6. Most of the resulting orbits are extremely eccentric, making Hercules to pass through the Disk and Bulge of the MW. Figure 7 shows the orbit for case A with $R_{\rm per}$=5.7 kpc and $R_{\rm apo}$=224 kpc.

Table 4: Candidates for the present velocity of Hercules

Case	A	B,E,F,G	C	D
v_t [$\mathrm{km\,s^{-1}}$]	-16	16	38	10
V_X [$\mathrm{km\,s^{-1}}$]	-108.1	-94.9	-85.8	-97.4
V_Y [$\mathrm{km\,s^{-1}}$]	-63.2	-48.1	-37.7	-50.9
V_Z [$\mathrm{km\,s^{-1}}$]	74.4	99.3	116.4	94.6

4.2 The Milky Way Potential

In our models we describe the potential and the resulting gravitational forces of the MW on the dwarf using two sets of analytical potentials:

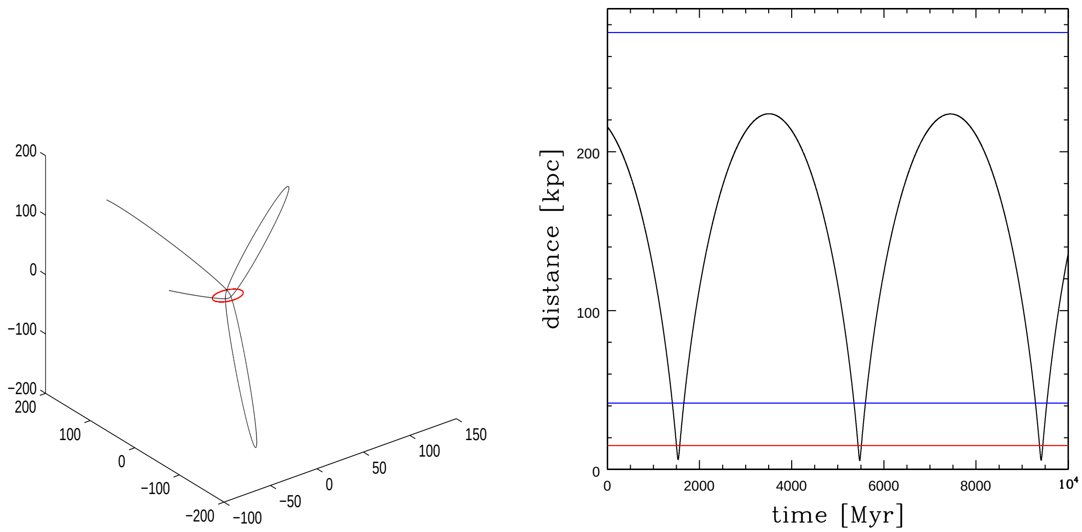

Figure 7: *Left*: The red projected circle corresponds to a diameter of 30 kpc around the Milky Way (MW). We plot in black colour the orbit of Hercules for cases A. *Right*: The red line indicates the radius of 15 kpc of the circle. We plot in black the evolution in time of the radial distance of Hercules respect to the centre of the MW. The upper blue line corresponds to the virial radius of a NFW halo of the MW (275 kpc) and the lower blue line corresponds to the scale radius of this halo (41.67 kpc). This orbit has a high eccentricity with a pericentre of R_{per}=5.7 kpc and an apocentre of R_{apo}=224 kpc.

4.2.1 Set (i)

We use the same setup as used by Jin & Martin (2010). A Miyamoto-Nagai profile for the disk, defined by Paczyński (1990):

$$\Phi_{disk}^{Pa}(R,z) = \frac{-GM_{Pa}}{\left(R^2+\left[a+(z^2+b^2)^{1/2}\right]^2\right)^{1/2}} \tag{10}$$

where $R^2 = x^2 + y^2$, with the parameters $a = 3.7$ kpc, $b = 0.2$ kpc and $M_{Pa} = 8.07 \times 10^{10}$ M$_\odot$.

For the bulge we use a Plummer profile also defined by Paczyński (1990):

$$\Phi_{bulge}^{Plum} = \frac{-GM_2}{\sqrt{r^2+r_{Pl}^2}} \tag{11}$$

with $r_{Plum} = 0.277$ kpc and $M_2 = 1.12 \times 10^{10}$ M$_\odot$.

Table 5: Initial conditions for the N-Body simulations for different cases

Case	A	B	C	D	E	F	G
t [Gyr]	-10	-10	-10	-10	-2.6	-5	-10
X [kpc]	-192.7	-98.6	-103.4	-89.1	145.3	-26.4	-143.9
Y [kpc]	-96.6	70.5	-22.6	139.7	168.4	-77.8	56.2
Z [kpc]	8.6	180.3	168.4	142.5	25.8	-87.8	37.6
V_X [km s^{-1}]	32.3	21.5	51.3	16.0	6.5	23.6	81.4
V_Y [km s^{-1}]	16.8	-7.6	22.9	-17.8	2.3	98.5	-26.4
V_Z [km s^{-1}]	-15.2	-26.0	-50.4	-16.6	-8.4	123.1	-6.1

Table 6: Minimum Pericenter and maximal apocenter for different cases (orbits) of Hercules.

Case	A	B	C	D	E	F	G
v_t [km s^{-1}]	-16	16	38	10	16	16	16
t [Gyr]	-10	-10	-10	-10	-2.6	-5	-10
R_{peri}^{min} [kpc]	5.7	3.3	11.8	1.8	3.9	3.9	2.4
R_{apo}^{max} [kpc]	224.0	224.2	229.2	223.5	224	224	174

And for the DM halo potential, we use an adiabatically contracted Navarro-Frenk-White halo constrained by Xue et al. (2008):

$$\Phi_{halo}^{NFW}(r) = -4\pi G r_s^3 \left[\frac{\ln(1+r/r_s)}{r} - \frac{1}{r_c+r_s}\right] \quad (12)$$

with $r_s = 41.67$ kpc, $r_c = r_{vir} = 275$ kpc and $M_{NFW} = \frac{4\pi}{3}\rho_{\rm cr}\Omega_m\delta_{\rm th}r_{vir}^3 = 1\times10^{12}$ $M_\odot$.

4.2.2 Set (ii)

For case G we use the standard description of the MW potential. A Miamoto-Nagai potential for the disk (Miyamoto & Nagai , 1975).

$$\Phi_{disk}^{MN}(R,z) = \frac{-GM_{MN}}{\left(R^2+\left[a+(z^2+b^2)^{1/2}\right]^2\right)^{1/2}} \quad (13)$$

where $R^2 = x^2+y^2$, with the parameters $a = 6.5$ kpc, $b = 0.26$ kpc and $M_{MN} = 1\times10^{11} M_\odot$.

A Hernquist profile for the bulge:

$$\Phi_{bulge}^{H} = \frac{-GM_H}{r+r_H} \quad (14)$$

with $r_H = 0.7$ kpc and $M_H = 3.34\times10^{10}$ $M_\odot$.

And for the DM halo potential, we used a logarithmic profile:

$$\Phi_{halo}^{Log}(r) = \frac{v_0^2}{2}\ln\left(r^2+d_{Log}^2\right). \quad (15)$$

with $v_0 = 186\,\mathrm{km\,s^{-1}}$ and $d_{Log} = 12\,\mathrm{kpc}$.

4.3 Possible Progenitors

We have two plausible scenarios for the progenitor: a DM-free or a DM-dominated dSph. As we use an orbit which is calculated assuming that Hercules has undergone a severe tidal disruption producing tidal tails that follow the orbit, we can neglect the scenario in which Hercules is still in equilibrium and highly dark matter dominated. For this reason and to reduce the parameter-space of possible initial conditions, we focus in this work on one-component models assuming the DM is already stripped or was not there from the beginning (TDG). We do not claim that Hercules has to be a TDG. But in order to validate the published, tentative orbit, which is based on tidal distortions, we are able to restrict ourselves to models starting out DM-free from the beginning. Also it is important to mention, that because of the high mass of the MW compared to Hercules, the orbit do not depend on the amount of mass in Hercules, whether it is constitute by DM or not.

We have two plausible endpoints of our simulation: namely a tidally distorted dwarf, where the high velocity-dispersion is caused by unbound stars and would also easily explain the measured velocity gradient; or we still see an object which is highly DM dominated and in virial equilibrium. Here the velocity dispersion is caused by the high DM content. Then the elongation and velocity-gradient are not due to tidal forces of the Milky Way, but are intrinsic properties of Hercules.

We adopt a Plummer sphere for the distribution of the stars, with $\rho_0 = \frac{3M_{pl}}{4\pi r_{pl}^3}$:

$$\rho_{pl}\left(r\right) \quad = \quad \frac{\rho_0}{\left(1+\left(r/r_{pl}\right)^2\right)^{5/2}} \tag{16}$$

having two parameters which we can fit: the initial scale-length or Plummer radius of the Plummer sphere R_{pl} and the initial mass M_{pl}.

We choose a *mass-to-light* ratio for the luminous mass of M^{stars}/ L$_V$=1 $\left[\frac{M_\odot}{L_\odot}\right]$ to calculate the surface-brightness.

5 Results and Discussion

We perform more than 600 simulations in order to cover the full parameter-space of the initial mass and the initial size of our model for Hercules to match the observations. In Table 7 we show the observable quantities we try to match: μ_0 is the central surface-brightness, M$_{fin}$ is the final mass with $M^{\rm stars}/L_{\rm V} = 1.39 \left[\frac{M_\odot}{L_\odot}\right]$, $r_{\rm h}$ is the projected half light radius, $\sigma_o^{\rm los}$ is the central line-of-sight velocity dispersion, Δv_r the radial velocity gradient, ε the ellipticity and θ the angle of inclination of the more elongated axis of the galaxy with respect to the axis of declination.

Table 7: Observational properties of Hercules (Adén et al., 2009a): μ_0 is the central surface-brightness, $M_{\rm fin}$ is the final mass with $M^{\rm stars}/\ L_{\rm V} = 1.39 \left[\frac{M_\odot}{L_\odot}\right]$, $r_{\rm h}$ is the projected half light radius, $\sigma_{\rm los}$ is the line-of-sight velocity-dispersion, $\Delta v_{\rm r}$ the radial velocity-gradient, ε the ellipticity and θ the angle of inclination of the elongation of the galaxy with respect to the axis of declination. For (*) we use the two most separated stars of Adén et al. (2009b), separated by $\Delta\alpha$ =0.35$^{\rm o}$.

Central surface-brightness	$\mu_{\rm o}$	27.2 ± 0.6 [mag arcsec^{-2}]
Final mass	$M_{\rm fin}$	$5.0 \pm 1.5 \times 10^4$ [M$_\odot$]
Projected half-light radius	$r_{\rm h}$	230 ± 30 [pc]
Ellipticity	ε	0.67 ± 0.03
Angle of inclination of the major axis	θ	$-78^{\rm o} \pm 4^{\rm o}$
Central Line-of-sight velocity-dispersion	$\sigma_{\rm o}^{\rm los}$	3.72 ± 0.91 [km s^{-1}]
Radial velocity-gradient	$\Delta^{0.35^{\rm o}} v_{\rm r}$	-7 ± 11 [km s^{-1}](*)

For each Case we fix 3 parameters: the potential for the MW, the infall time, and the tangential velocity. And we vary the total initial mass M$_{tot}^{init}$ of the Plummer sphere (the model for Hercules) and the Plummer radius, R$_{Pl}$. We then plot for each of the 7 cases (A through G), the initial total mass M$_{tot}^{init}$ versus the 7 observable quantities mentioned before. For case A we repeat the procedure leaving the initial mass fixed and varying the Plummer radius versus the observable quantities.

In this section we focus on the results of Case A and as mentioned before the orbit of Case A was proposed by Jin & Martin (2010) and we used an infall-time of 10 Gyr. We show the results of Case A in Tab. 8. We show in the Appendix the tables of the results of Cases B and C, and the plots of the results of Cases B, C, D, E, F and G.

We divide the analysis in 3 sets of observational parameters for explanatory purpose:

1 Luminosity and Size: The final luminous mass M$_{fin}$, central surface-brightness μ_o and effective radius R$_{eff}$.

2 The Shape and Orientation: The ellipticity ε and angle of alignment θ.

3 The Kinematics: The central velocity-dispersion $\sigma_{\rm los}^{0.4^o}$ and the radial velocity-gradient $\Delta^{0.4^o} v_r$.

Table 8: Results of Case A. This table contains the results for the orbit proposed by Jin & Martin (2010), the Galactic potential they used and an orbital time of 10 Gyr. The first column is the name of the simulation, the second corresponds to the initial total mass of the Plummer distribution. The third column is the initial Plummer radius. In the fourth and fifth columns we show the final mass $M_{\rm fin}$ and the final central surface-brightness respectively where we use a $M^{\rm stars}/L_{\rm V} = 1\left[\frac{M_\odot}{L_\odot}\right]$. The sixth column is the final effective radius $r_{\rm h}$ fitted with a Sersic-profile. The seventh column is the angle of inclination θ of the elongation respect to the axis of declination (δ). The eighth column is the final ellipticity of the dwarf galaxy. The ninth is the final line-of-sight velocity dispersion and finally the last column corresponds to the radial velocity gradient in $\Delta\alpha = 0.4^{\rm o}$ which is a distance in the axis of the right ascension.

N$^{\rm o}$	$\rm M_{init}$ [$\rm M_\odot$]	$\rm R_{Pl}$ [pc]	$\rm M_{fin}$ [$\rm M_\odot$]	$\mu_{\rm o}$ $\left[\frac{\rm mag}{\rm arcsec^2}\right]$	$\rm r_{eff}$ [pc]	θ [$^{\rm o}$]	ε	$\sigma_{\rm los}^{0.4^o}$ $\left[\frac{\rm km}{\rm s}\right]$	$\Delta^{0.4^o} v_r$ $\left[\frac{\rm km}{\rm s}\right]$
	Hercules		5.0E+4	27.2	230	-78	0.67	3.72	-8
H06	5.0E+4	50	1.4E+4	29.5	293	-145	0.37	3.91	-4.5
H07	1.0E+5	50	3.8E+4	26.2	56	-73	0.20	2.45	-3.2
H08	2.0E+5	50	1.1E+5	24.0	44	-78	0.04	1.85	-2.5
H09	5.0E+5	50	3.7E+5	22.2	40	-70	0.00	2.09	0.0
H10	1.0E+6	50	8.4E+5	21.2	40	-75	0.03	2.90	0.0
H11	5.0E+4	60	6.8E+3	31.5	1624	-78	0.14	6.39	-8.0
H12	1.0E+5	60	2.2E+4	28.7	351	-150	0.35	3.66	-2.9
H13	2.0E+5	60	7.9E+4	25.2	55	-70	0.02	2.33	-3.2
H14	5.0E+5	60	3.1E+5	23.0	51	-70	0.05	2.00	0.0
H15	1.0E+6	60	7.5E+5	21.8	48	-70	0.00	2.60	0.0
H16	5.0E+4	80	5.3E+3	31.7	1021	-140	0.30	6.91	-6.5
H17	1.0E+5	80	9.4E+3	31.6	1641	-78	0.15	8.00	-11.0
H18	2.0E+5	80	2.9E+4	29.1	439	-145	0.42	4.82	-2.5
H19	5.0E+5	80	1.9E+5	24.8	77	-75	0.08	2.44	-2.5
H20	1.0E+6	80	5.5E+5	23.0	68	-75	0.07	2.28	0.0
H21	5.0E+4	100	3.0E+3	32.8	1600	-130	0.36	10.26	-4.5
H22	1.0E+5	100	8.1E+3	31.3	1084	-130	0.26	8.12	-6.5
H22b	2.0E+5	100	1.2E+4	31.4	1084	-130	0.00	9.83	-7.5
H23	5.0E+5	100	8.9E+4	27.6	586	-70	0.11	4.04	-2.7
H24	1.0E+6	100	3.6E+5	24.8	98	-70	0.07	2.60	1.2

5.1 Luminosity and Size

5.1.1 Final Mass

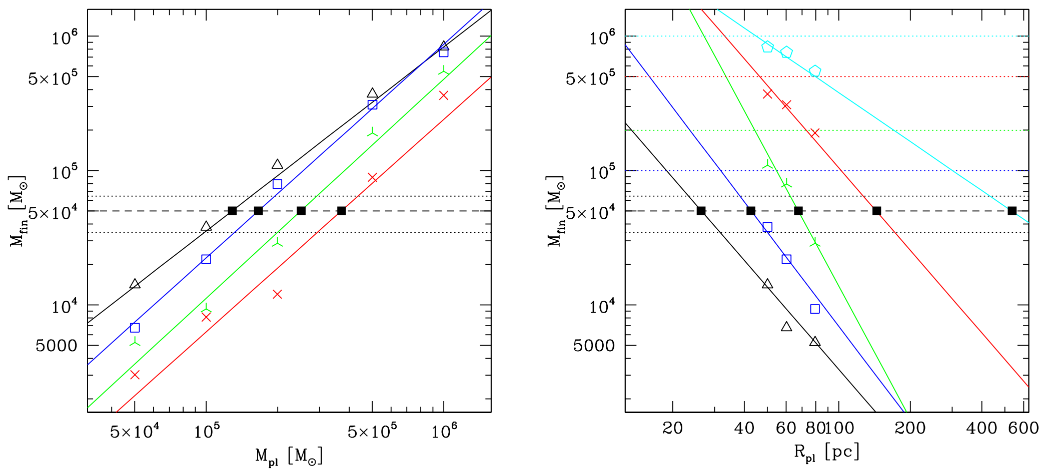

Figure 8: *Left*: We plot the value of the final mass within a 500 pc box ($M_{\rm fin}$) versus the initial mass ($M_{\rm pl}$) for case A. Black open triangles denote simulations with Plummer radius of 50 pc, blue open squares 60 pc, green tri-pods 80 pc and finally red crosses 100 pc. The lines are power-law fits to the results and black filled squares denote the points where these fits match the observations. *Right*: Final mass ($M_{\rm fin}$) versus initial Plummer radius. The black open triangles represent simulations with initial mass of 5×10^4 $M_\odot$, the blue open squares 10^5 $M_\odot$, green tri-pods 2×10^5 $M_\odot$, red crosses 5×10^5 $M_\odot$ and cyan open symbols represent 10^6 $M_\odot$. Solid lines are the fits to the data and pointed lines are the values which correspond to the initial mass. The black dotted line is the observed value: $5 \pm 1.5 \times 10^4 M_\odot$. Again black filled squares represent the values where the fitted lines meet the observed values.

As we already mention in subsection 2.2, when a dwarf galaxy orbits around a massive galaxy like the MW, it suffers from tidal disruption which produces a mass-loss. We search for a final mass that matches the observed value of Hercules, $\sim 5 \times 10^4$ $M_\odot$. In the left panel of Fig. 8 we show, for case A, how the final mass of the galaxy changes with the initial mass, while the different symbols and colours correspond to simulations with different initial Plummer radius. As we mentioned, the masses we analyzed here correspond just to luminous mass, and no DM. For very low initial masses (below $\sim 10^5$ [$M_\odot$]) the galaxy gets unbound very fast, using Plummer radii larger than 50 pc, turning the particle distribution into a stream with very low final masses ($\sim 10^3$ $M_\odot$ or less). For high initial masses, over $\sim 5 \times 10^5$ $M_\odot$ and Plummer radii between 50 pc and 100 pc, the final mass tends to be the same as the initial. Our region of interest lies somewhere in between. In our log-log plot (left panel of Fig. 8) we see that the relation between initial and final mass follows similar power-laws with indexes between 1.37 (50 pc) and 1.63 (80 pc). But we know that we can not use all data points for our fits. At the high mass end, the tendency should converge closer to a relation

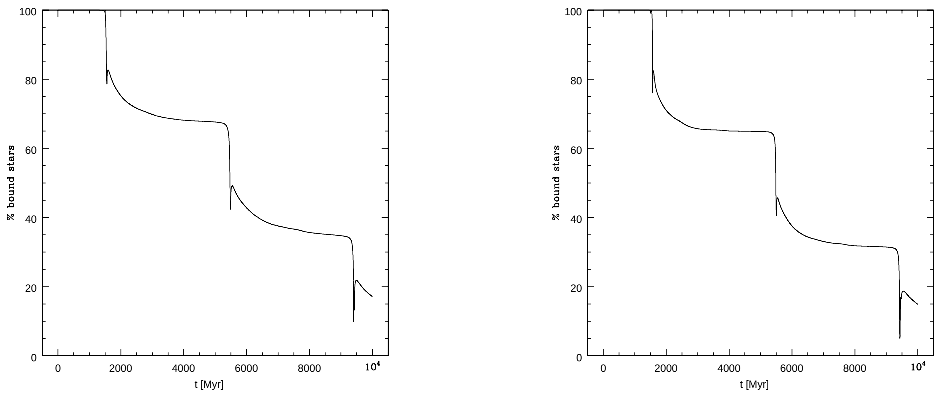

Figure 9: The evolution with time of the bound fraction of mass for simulations of cases A and B. *Left*: simulation H36 for case A (with $v_t = -16\,\mathrm{km\,s^{-1}}$). *Right*: Simulation 483c for case B (with $v_t = (+)16\,\mathrm{km\,s^{-1}}$). Both orbits are different, but at the final point of the orbits both have movements along the direction of the actual observed elongation in Hercules, and differ in the sign of the direction. The number of passages through the pericenter is the same and the mass-loss is equally strong.

1:1, because the final mass can never be larger than the initial mass. And at the low mass end we also expect a deviation from the power-law as the simulations tend to form a uniform stream and so we should expect almost the same mass in the field of view, independent from the initial model. In the right panel of Fig. 8 we see the deviation at the low-mass end for large Plummer radii clearly.

In the right panel of the same figure (Fig.8) we show the same simulations but now we plot the initial Plummer radius versus the final mass and show curves with the same initial mass. Here again we see that the results in the intermediate regime follow power-laws with indexes -2.04 to -3.28. In this plot we see clearly the deviation from the power-laws towards the relation that the initial mass equals final mass.

We use the intermediate values (values near the observed value) to extrapolate for both plots separately, the fitting values to match the observed mass of Hercules. The matching values are indicated in the plots by black filled squares. In the left panel we get $M_{\mathrm{fit}} = 1.29\times10^5$ M$_\odot$ for $R_{\mathrm{pl}} = 50$ pc, $M_{\mathrm{fit}} = 1.66\times10^5$ M$_\odot$ for $R_{\mathrm{pl}} = 60$ pc, $M_{\mathrm{fit}} = 2.50\times10^5$ M$_\odot$ for $R_{\mathrm{pl}} = 80$ pc, and $M_{\mathrm{fit}} = 3.71\times10^5$ M$_\odot$ for $R_{\mathrm{pl}} = 100$ pc. In the right panel the fitting values are $R_{\mathrm{fit}} = 26.4$ pc for $M_{\mathrm{ini}} = 5\times10^4$ M$_\odot$, $R_{\mathrm{fit}} = 42.7$ pc for $M_{\mathrm{ini}} = 10^5$ M$_\odot$, $R_{\mathrm{fit}} = 67.5$ pc for $M_{\mathrm{ini}} = 2\times10^5$ M$_\odot$, $R_{\mathrm{fit}} = 143.5$ pc for $M_{\mathrm{ini}} = 5\times10^5$ M$_\odot$, and finally $R_{\mathrm{fit}} = 533.6$ pc for $M_{\mathrm{ini}} = 10^6$ M$_\odot$.

We can use these fitted values to compute a power-law relation for the pairs of initial Plummer radii and masses, which lead to a match of the final mass of Hercules. The two relations are:

$$M_{\mathrm{ini}} = 316.2 R_{\mathrm{pl}}^{1.53}, \quad (17)$$

$$R_{\mathrm{pl}} = \frac{M_{\mathrm{ini}}^{0.96}}{1259} \quad (18)$$

respectively. We will come back to these relations in a section further below, when we discuss our best matching models for Hercules.

The mass-loss process is roughly explained by Eq. 8, as in each pass of the dwarf galaxy through the pericenter of the orbit, the tidal radius strongly shrinks, making that several stars in the dwarf galaxy located outside this radius get gravitationally unbound by the Milky Way, joining the stream structure. Other stars move back into the dwarf and get gravitationally rebound as it travels towards the apocentre. We choose simulations H36 and Sim483c of cases A and B respectively to show the mass-loss process in action in Fig. 9, where each drop in the curve of the panels in the Figure is a pass of the Hercules through the pericenter. Both simulations have similar final size, surface-brightness and final mass to the ones observed in Hercules, but differs in their kinematics. The number of passages through the pericenter is the same and the mass-loss produced by the small pericenter is equally high.

5.1.2 Surface Brightness

As the dwarf galaxy orbits, it looses mass and expands, making it fainter. To calculate the surface-brightness we use a $M^{\rm stars}/L_{\rm V} = 1 \left[\frac{M_{\odot}}{L_{\odot}}\right]$. We show some surface-brightness contours of Case A in Fig. 10, where we show the three dynamical regimes for the dwarf galaxy that we could identify, when our simulations finished and reached the present time:

1 Bound Regime (BR): the particles are very concentrated and tightly bound in a core.

2 Tidal Regime (TR): the particles in the core are more extended than in the BR, but it is still bound.

3 Unbound Regime (UR): there is no core and the particles are totally unbound, forming an extended stream along the orbit with very low surface-brightness.

We show in the left panel of Fig. 11 the changes in the surface-brightness as we increase the initial total mass at fixed Plummer radii, which are indicated with triangles of the same colour (see figure caption for details). And in the right panel, the changes in the surface-brightness with different Plummer radii at constant initial masses are shown (also indicated with triangles of the same colour). In this panels we see two transitions: from the bound regime to the tidal regime, and then from the tidal regime to the unbound regime. For higher surface-brightnesses (or higher concentrations) than the observed value, the increasing ratio (see the slope) of the surface-brightness is slow as we increase the initial mass (left panel) or as we decrease the Plummer radii (right panel). Around the observed value the increasing ratio is fast. Here again we use the data points to extrapolate the matching values of initial conditions (M_{init} and R_{Plum} to achieve the central surface brightness of Hercules at the end of the simulations. Note especially that in the left log-log plot the relations are self-similar as the fitting lines are almost parallel to each other. We use these matching points and again calculate fitting power-laws to the matching values. Again we discuss these fits in a following section.

In the simulations with results below the observed values, the surface-brightness decreases very slowly with decreasing mass (left panel) or increasing Plummer radius (right

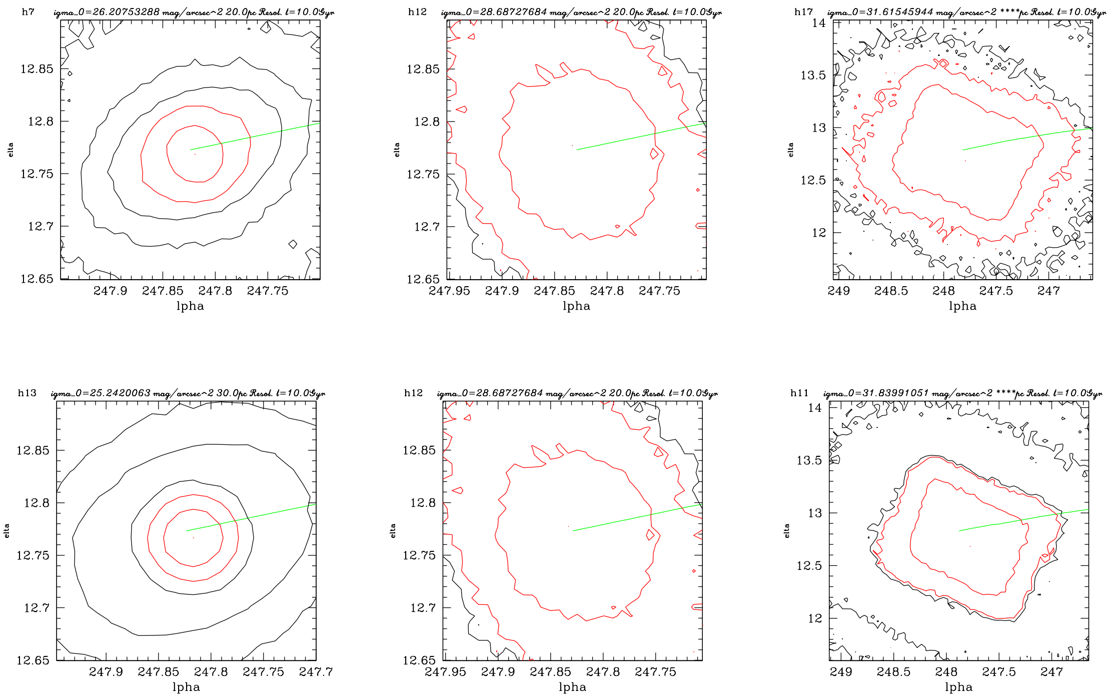

Figure 10: The surface-brightness contours of some simulations of case A, which show the 3 regimes that we may get. The projection of the orbit is showed with a green line. The central surface-brightness is indicated at the top of each panel and the red and black contours indicate the decrease of the apparent magnitude by one magnitude. In the first three *upper-row* panels we plot the cases with constant initial mass ($M_{\rm ini} = 10^5$ M$_\odot$) but with different initial Plummer radius R$_{Pl}$: *upper-left* 50 pc, *upper-centre* 60 pc and *upper-right* 80 pc. For the *Bottom row* panels we fix the Plummer radius ($R_{\rm pl} = 60$ pc) and we vary the total initial mass. M$_{init}$: *bottom-left* 2×10^5 M$_\odot$, *bottom-centre* 10^5 M$_\odot$ and *bottom-right* 5×10^4 M$_\odot$. The left panels show the galaxy under a bound regime (BR), the middle panels show a tidal regime (TR) and the right panels show the unbound regime (UR). (Note that the scale of the figures *upper-right* and *bottom-right* have a size of 2.5$^{\rm o}$ (3 kpc), while the other four panels have 0.25$^{\rm o}$ (0.3 kpc) only).

panel). Here we are in the unbound regime and we are dealing with a tidal stream without any bound central object.

Comparing these results with the final mass from subsection 5.1.1 shown in Fig. 8, we may see that both quantities (mass and surface-brightness) increase proportionally with the initial mass.

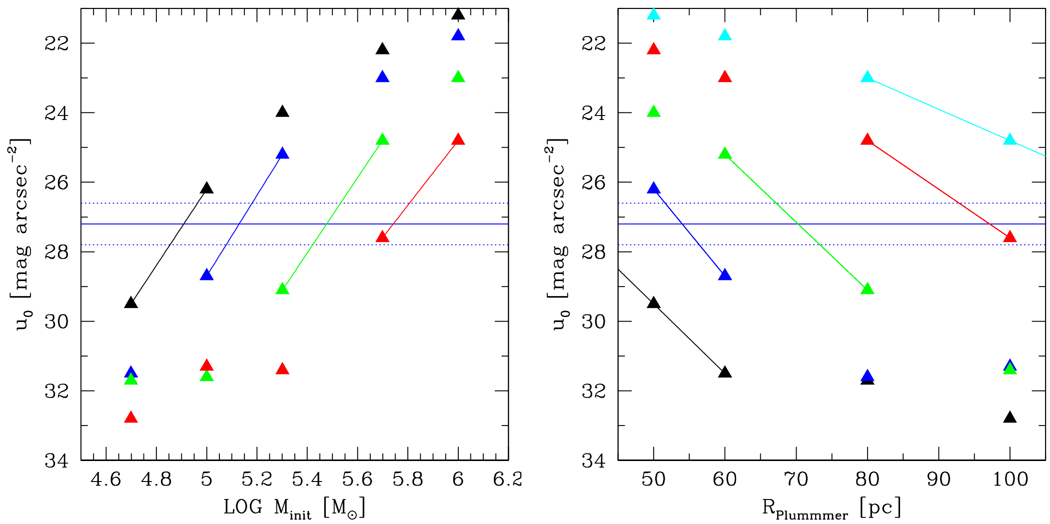

Figure 11: *Left*: We plot the values for the central surface-brightness (μ_o) versus the initial total mass ($M_{\rm ini}$), each triangle correspond to a simulation for case A. The colours indicate the Plummer radius: black 50 pc, blue 60 pc, green 80 pc and red 100 pc. *Right*: Central surface-brightness (μ_o) versus the initial Plummer radii. The coloured triangles indicate different initial total masses: black 5×10^4 M$_\odot$, blue 10^5 M$_\odot$, green 2×10^5 M$_\odot$, red 5×10^5 M$_\odot$, and cyan 10^6 M$_\odot$. The horizontal blue lines correspond to the observed value: $\mu_o = 27.0 \pm 0.6$ mag arcsec^{-2}. The coloured lines are extrapolations to determine the values for the initial total mass and Plummer radius that would match the observed final surface-brightness.

5.1.3 Effective Radius.

We use the surface-brightness contours of our simulations, to calculate a surface - brightness profile with radial bins to fit a Sérsic-profile $\mu_{\rm Ser}(r)$ for each simulation. From this profile we get a projected effective radius $r_{\rm eff}$, which we then compare with the observed half-light radius of Hercules.

We already mentioned that each passage through the pericenter makes the galaxy more extend than its original size. The growth is slow under the bound regime until it reaches the tidal regime. Here it expands fast until it reaches the unbound regime, where the galaxy explodes and becomes only a stream. We may see this change of regime in Fig. 12: the left panel with the initial mass (M_{init}) and the final size (R_{eff}) shows the slow growth at sizes of $\sim 10^3$ pc for the unbound regime as we decrease the initial mass. Then a fast growth at sizes of $\sim 10^2$ pc and finally again a slow growth at sizes of ~ 10 pc. When the galaxy is unbound and becomes a stream, the effective radius is not a good parameter, because there is no symmetric radius, and instead it is just a more or less equal density stream along the orbit that gets thinner and longer across the path of the orbit with time.

The right panel in Fig. 12 shows the three expansion rates for the three regimes as we change the Plummer radius. This panel reveals that the more mass we put into the same Plummer radius, the smaller the effective radius will be. Putting more mass into the same

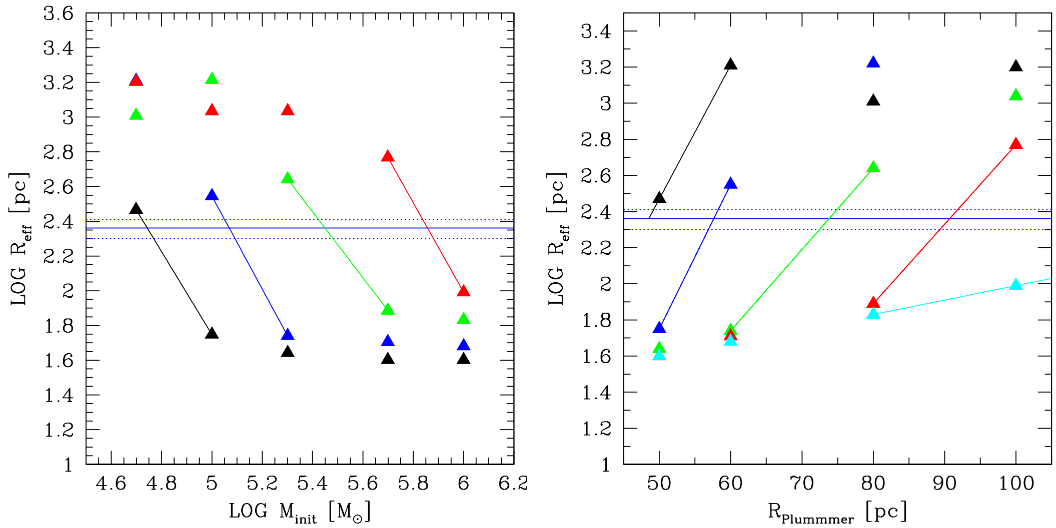

Figure 12: *Left*: We plot the effective radius ($r_{\rm h}$) versus the initial mass ($M_{\rm ini}$). Each triangle corresponds to a simulation of case A. The colours indicate the Plummer radius: black 50 pc, blue 60 pc, green 80 pc and red 100 pc. *Right*: Effective radius ($r_{\rm h}$) versus the initial Plummer radius. Colours indicate different initial masses: black 5×10^4 M$_\odot$, blue 10^5 M$_\odot$, green 2×10^5 M$_\odot$, red 5×10^5 M$_\odot$, and cyan 10^6 M$_\odot$. The horizontal blue lines correspond to the observed value: $r_{\rm h} = 230 \pm 30$ pc or $\log(r_{\rm h}) \approx 2.36$. The coloured lines are extrapolations to determine the values for the initial mass and Plummer radius that match the observed effective radius.

Plummer radius makes the initial Plummer sphere more concentrated, which makes it harder to disrupt by the MW potential.

Once more we determine the values of initial conditions which lead to the matching effective radii at the end of the simulations by extrapolating the intermediate data points of our simulations.

5.2 Shape and Orientation

5.2.1 Angle of Inclination

In Figure 15 we plot the total initial mass versus the angle of inclination of the elongation of the object with respect to the axis of declination. We notice that the angle of inclination is not always aligned with the angle of the orbit (-78$^{\rm o}$) (blue horizontal line in the figure), but it strongly depends on the amount of final mass. The stars are located in three zones within the dwarf galaxy. The gravitationally unbound zone, which represents the external or sourrounding distribution of stars which follow the path of the orbit. Then, further inwards the tidal zone, where the stars are escaping from the bound zone. In all our cases the projected distribution of stars in this zone lies almost perpendicular to the plane of the orbit. Therefore in some cases the angle of the major axis is 0$^{\rm o}$. This happens because after each passage through the pericenter the new unbound stars need some time to align with the orbit. More

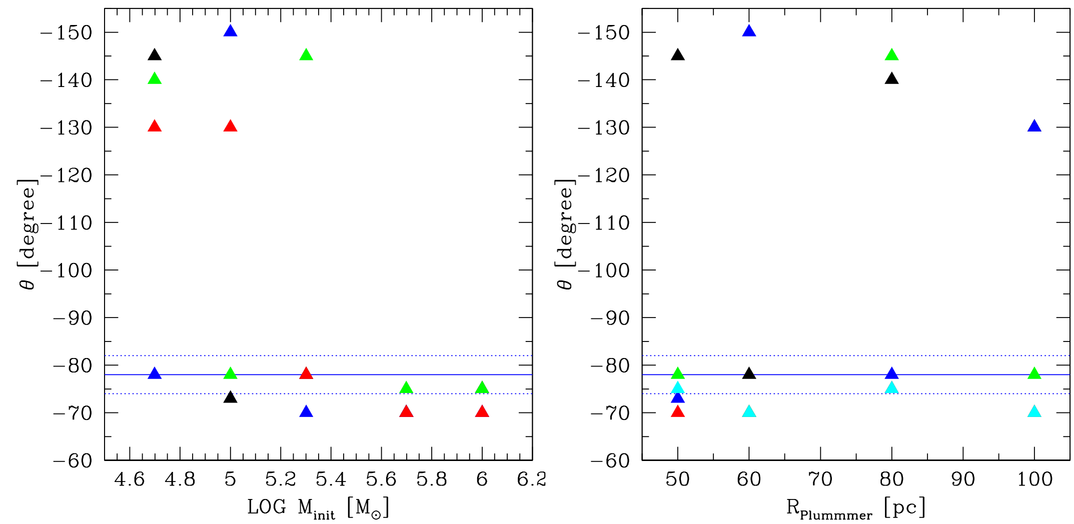

Figure 13: *Left*: We plot the angle of inclination (θ) versus the initial mass ($M_{\rm ini}$). Each triangle corresponds to a simulation of case A. The colours indicate the Plummer radius: black: 50 pc, blue 60 pc, green 80 pc, and red 100 pc. *Right*: Angle of inclination (θ) versus the initial Plummer radius. The coloured triangles indicate different initial total masses: black 5×10^4 M$_\odot$, blue 10^5 M$_\odot$, green 2×10^5 M$_\odot$, red 5×10^5 M$_\odot$, and cyan 10^6 M$_\odot$. The blue horizontal line corresponds to the observed value: $\theta = -78^{\rm o} \pm 4^{\rm o}$.

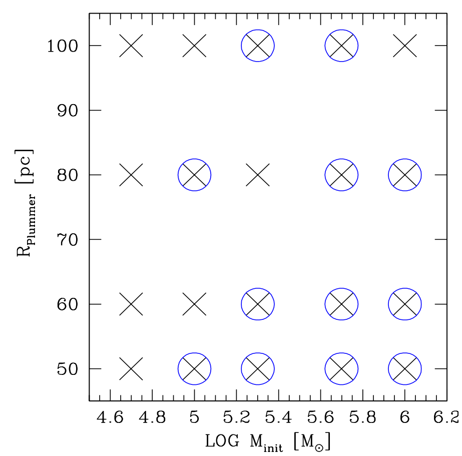

Figure 14: We plot for case A the investigated parameter space, where a cross represents a performed simulation. Whenever we match the observational angle of inclination by ± 10 per cent we place a circle around the cross. We choose this slightly different representation because there are no clear power-law dependencies which could match the different data points.

details of this delay in the alignment is explain in Klimentowski et al. (2009). The third zone is the core where the stars are still gravitationally bound. The elongation in this zone is not exactly along the orbit either, but in some cases it differs by only $10^{\rm o}$.

We choose to measure the angle of inclination at the range of declination which corre-

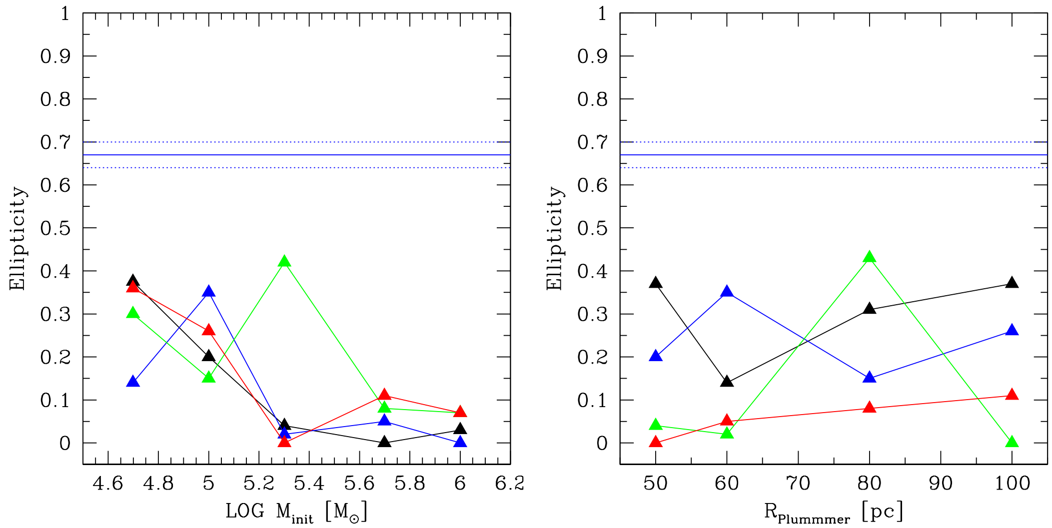

Figure 15: *Left*: Ellipticity (ε) versus the initial mass. Each triangle corresponds to a simulation of case A. The colours indicate the Plummer radius: black 50 pc, blue 60 pc, green 80 pc, and red 100 pc. *Right*: Ellipticity (ε) versus the initial Plummer radius. The coloured triangles indicate different initial total masses: black 5×10^4 $M_\odot$, blue 10^5 $M_\odot$, green 2×10^5 $M_\odot$, red 5×10^5 $M_\odot$, and cyan 10^6 $M_\odot$. The horizontal blue lines correspond to the observed value: $\varepsilon = 0.67 \pm 0.03$.

sponds to the extension of the observed dwarf galaxy, i.e. in the same range the observers determine the angle θ. For this reason, it depends strongly on the simulation if we find ourselves in the unbound, tidal or bound region of the model. Therefore, we see strong variations in θ and are not able to fit any power-laws or similar dependencies to our results. We therefore choose to take into account as matches all the simulations with inclinations of -78 degrees or those that differ by only 10 per cent of this value. These values are denoted in Fig. 14 as circles.

Another interesting fact, we noted, is that the angle θ of the bound structure changes its alignment with the orbit, depending on the sign of the tangential velocity. Most of the cases with positive $v_{\rm tan}$ have angles that are $\theta < -78^{\rm o}$ and when $v_{\rm tan}$ is negative $\theta > -78^{\rm o}$. We may see this effect for simulations with initial masses higher than 10^5 $M_\odot$ in case A which has $v_{\rm tan} = -16$ km s^{-1} (see Fig. 13), and compare it with Cases B, C, D and G which have $v_{\rm tan} = 10$ km s^{-1} to 30 km s^{-1} (see Annex: Figure 25).

5.2.2 Ellipticity

The projected ellipticity is very difficult to match with the observed one in Hercules. In case A only a few simulations become as elliptical as Hercules, but they are totally unbound and are streams that are much more extended (> 3 kpc) than Hercules. None of the simulations could match the observed ellipticity within a range of ~ 20 per cent simultaneously with any other parameter. We show in Fig. 15 that within our range for the initial mass and Plummer radii, the ellipticity is always low. The projected ellipticity reaches a maximum value in a simulation if we measure in the tidal regime and then, as we explained earlier with the angle of inclination, the galaxy starts to get round again, as it expands perpendicularly to the orbit and to the previous elongation. It is continuosly expanding in the perpedicular direction until it again starts to expand along the elongation.

Because we only obtain final objects which are less flattened, we conclude that some of the final ellipticity might already been present in the initial model. As we just use spherical initial models for simplicity we drop this parameter from the list of parameters we try to match.

5.3 Kinematics

5.3.1 Line-of-Sight Velocity Dispersion

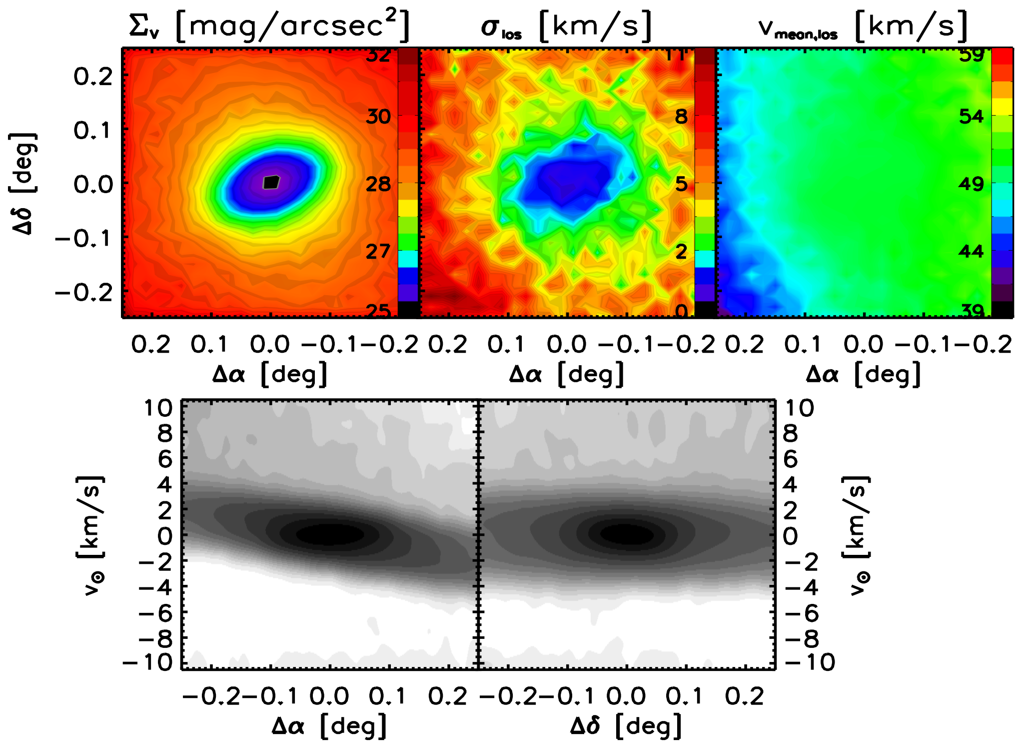

Figure 16: Final results after a 10 Gyr orbit for a simulation of case A, which is not mentioned in our grid of simulations. The initial mass for this simulation is 1.8×10^5 M$_\odot$ and the Plummer radius is 65 pc. The contours are based on 25 by 25 pixels. *Upper-left panel*: Surface-brightness contours, *Upper-central panel*: line-of-sight velocity dispersion contours, *Upper-right panel*: Contours of mean radial velocity, calculated for each pixel. *Bottom panels*: density maps of radial velocity versus the Right Ascension (α) and the Declination (δ).

In Fig. 16 we show the velocity dispersion contours of simulation h36 as an example. The bound core shows a low velocity dispersion and then it increases outwards, where the stars

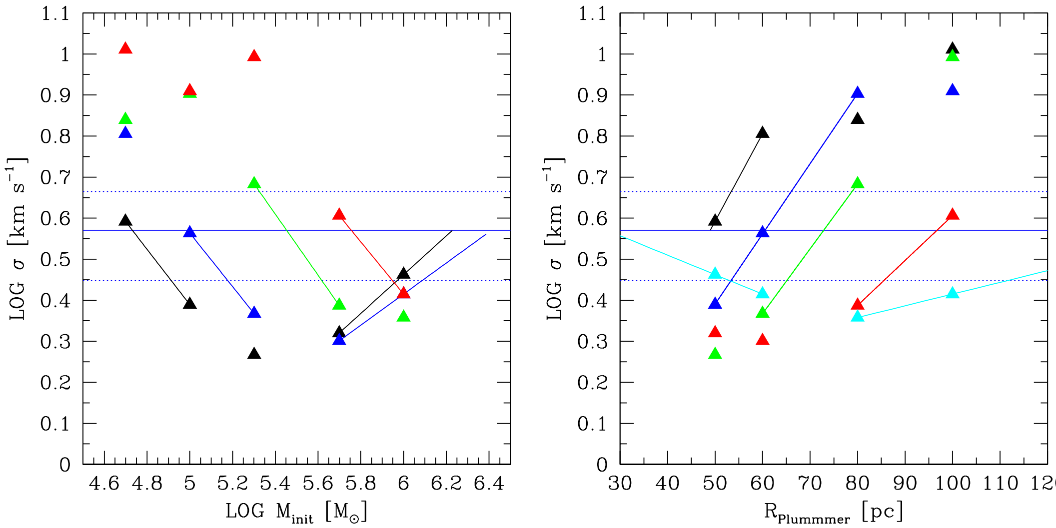

Figure 17: *Left*: Line-of-sight velocity dispersion $\sigma_{\rm los}$ versus initial mass. Each triangle corresponds to a simulation for case A. The colours indicate the Plummer radius: black 50 pc, blue 60 pc, green 80 pc, and red 100 pc. *Right*: σ_0^{los} versus the initial Plummer radius. The coloured triangles indicate different initial masses: black 5×10^4 M$_\odot$, blue 10^5 M$_\odot$, green 2×10^5 M$_\odot$, red 5×10^5 M$_\odot$, and cyan 10^6 M$_\odot$. The blue horizontal line corresponds to the observed value: $\sigma_{\rm los} = 3.7 \pm 0.91$ km s^{-1}. The coloured lines are extrapolations to determine the values for the initial total mass and Plummer radius that match the observed line-of-sight velocity dispersion.

are unbound. The central line-of-sight velocity-dispersion strongly depends on the bound to unbound ratio of stars in projection of the core. As long as the core is gravitationally bound and dense, the velocity-dispersion increases when we increase the initial mass, following the virial equilibrium relation (see Eq. 5). For cases where the core is unbound or of low density with respect to the unbound stars, the velocity-dispersion is higher than in the bound cases. This happens because the unbound stars are no longer in virial equilibrium and instead are moving in a streaming motion.

As there are just a handful of radial velocities observed throughout the whole body of Hercules, we do not compare the central velocity dispersion or the dispersion of the bound particles of our models with the data. Instead we calculate a 'mean' velocity dispersion in a 0.4 by 0.4 degree field centered on our object to cover the same space than the stars which have observed radial velocities and are thought to belong to Hercules. We use all our particles in this field irrespectively if they are bound or not to mimic the observationally derived value.

We see the effect of this method in Fig. 17, where for masses of $\approx 5 \times 10^4$ M$_\odot$ to $\approx 10^5$ M$_\odot$ and large Plummer radii the dispersion is high because of the streaming motion, and then the dispersion starts to get lower when a gravitationally bound core is present. And finally for higher masses (10^5 M$_\odot$ to 10^6 M$_\odot$) the dispersion starts to rise again according to the virial equilibrium conditions. If we look into the centre, we find a mix of stars in both regimes. The unbound stars have high velocity-dispersions, and they will inflate the velocity-dispersion of the bound stars. Therefore we have that the parameter space reaches the observed velocity dispersion twice depending on the regime. The less massive (i.e. less initial mass) solutions correspond to the tidal regime and the more massive ones to the bound regime, in which the objects are in virial equilibrium.

Again we extrapolate the results in the tidal and in the bound regime to assess the matching values of Hercules.

5.3.2 Radial Velocity-Gradient

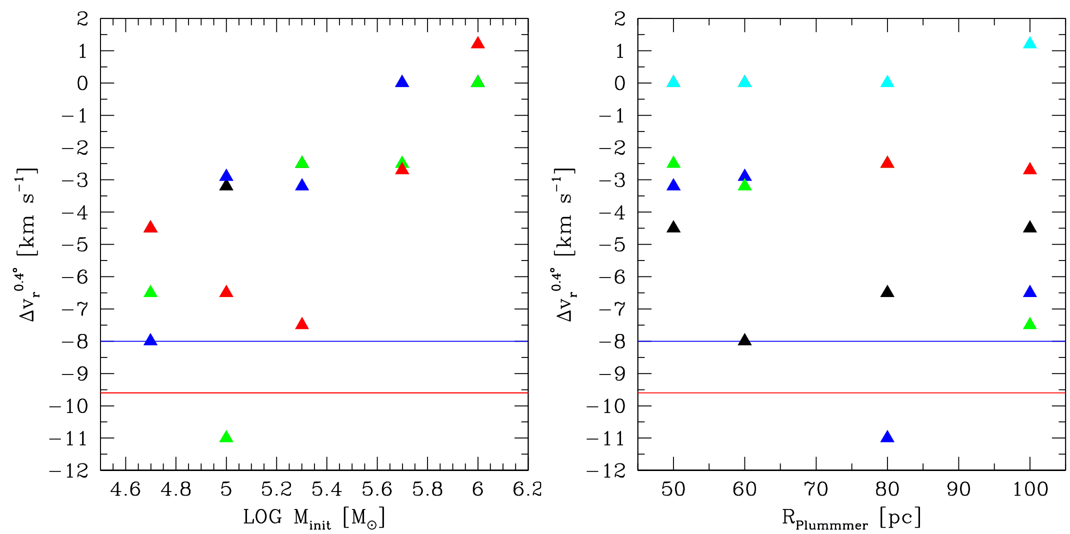

Figure 18: *Left*: We plot the radial velocity gradient $\Delta v_{\rm r}$ measured just along the Right Ascension axis within a width of $\Delta\alpha = 0.4^{\rm o}$ versus the initial mass. Each triangle corresponds to a simulation for case A. The colours indicate the Plummer radius: black 50 pc, blue 60 pc, green 80 pc, and red 100 pc. *Right*: $\Delta^{0.4^o} v_{\rm r}$ versus the initial Plummer radius. The coloured triangles indicate different initial masses: black 5×10^4 $M_{\odot}$, blue 10^5 $M_{\odot}$, green 2×10^5 $M_{\odot}$, red 5×10^5 $M_{\odot}$, and cyan 10^6 $M_{\odot}$. The blue horizontal line corresponds to the observed value: $\Delta^{0.4} v_r \approx$-8$\pm$12.6 km s^{-1}. The red horizonal line is the value estimated by Jin & Martin (2010).

The radial velocity-gradient is more complex to analyse, because it strongly changes depending on the zone where we are measuring it ($\Delta\alpha$). The fact that the alignment of the core, the tidal zone and the stream do not occur instantaneously generates an overlap for these three distributions (see lower panels of Fig. 16). This overlap can strongly affect the observations, changing the velocity gradient and also increasing the velocity-dispersion. The stars at the background of the panel that are more extended ($\Delta\alpha \sim 0.5^o$) are in the unbound regime, following the streaming motion. These stars have a high velocity-gradient (over ~ -10 km s^{-1}deg^{-1}) caused by their almost exclusive exposition to the MW potential gradient. In the tidal zone (about $\Delta\alpha \sim 0.2^o$ around the centre) the stars are more equally exposed to both gravitational fields and have a gradient of ~ -10 km s^{-1}deg^{-1}. Finally in the bound zone (if a core is present) the gradient disappears. This kinematic characteristic persists for simulations with different initial masses or Plummer radii. In Fig. 18 we show how the choice of the initial total mass and the initial Plummer radius for case A affects the velocity-gradient. Again we do not measure the velocity gradient of a specific regime but we use a fixed extension along the dwarf of ± 0.4 degrees. As in the case of the $theta$ parameter, we cannot fit simple power laws to our results and therefore will only use gradients higher than $\Delta^{0.4} v_r \leq -6$ km s^{-1}

5.4 A Matching Model for Hercules

We performe extrapolations in the plots for the final mass, surface-brightness, effective radius and the velocity dispersion to determine the initial masses and Plummer radii that match the observed values for those quantities. In Figures 8, 11, 12, and 17 we see the triangles near the blue horizontal line and the extrapolations that pass through this line. We then plot this values obtained from the extrapolations in Fig. 19 which represents the parameter space for the initial mass versus Plummer radius. The squares represent the values extrapolated from the constant mass plots and the triangles correspond to constant Plummer radius plots. The colours indicate observable parameter that they match. Black correspond to the final mass and blue is the final surface-brightness. Red is the effective radius and green represents the velocity dispersion. We then also plot as fill cyan circles the values for the initial masses and Plummer radii obtained from velocity-gradient values that match the observed value within a range of $\approx -21 \pm 5$ km s^{-1}deg^{-1}. The magenta circles are the values for the angle of inclination that match within a range of -70^{o} and -78$^{\mathrm{o}}$. Two solution regions for the velocity dispersion exist because they correspond to different regimes that generate the same dispersion but with different masses. The upper green line corresponds to the tidal regime and the bottom with more massive solutions is the bound regime in virial equilibrium.

All solutions converge/intersect around a range for the initial mass of between $M_{\mathrm{ini}} \approx 1.6 \times 10^5$ M$_\odot$ and 2.5×10^5 M$_\odot$ and for Plummer radii between $R_{\mathrm{pl}} = 68$ pc and 80 pc. In this region lies a unique model for Hercules which matches all the observable data. The exception is the ellipticity but this can be cured by introducing another parameter for the initial conditions covering any initial flattening of the model.

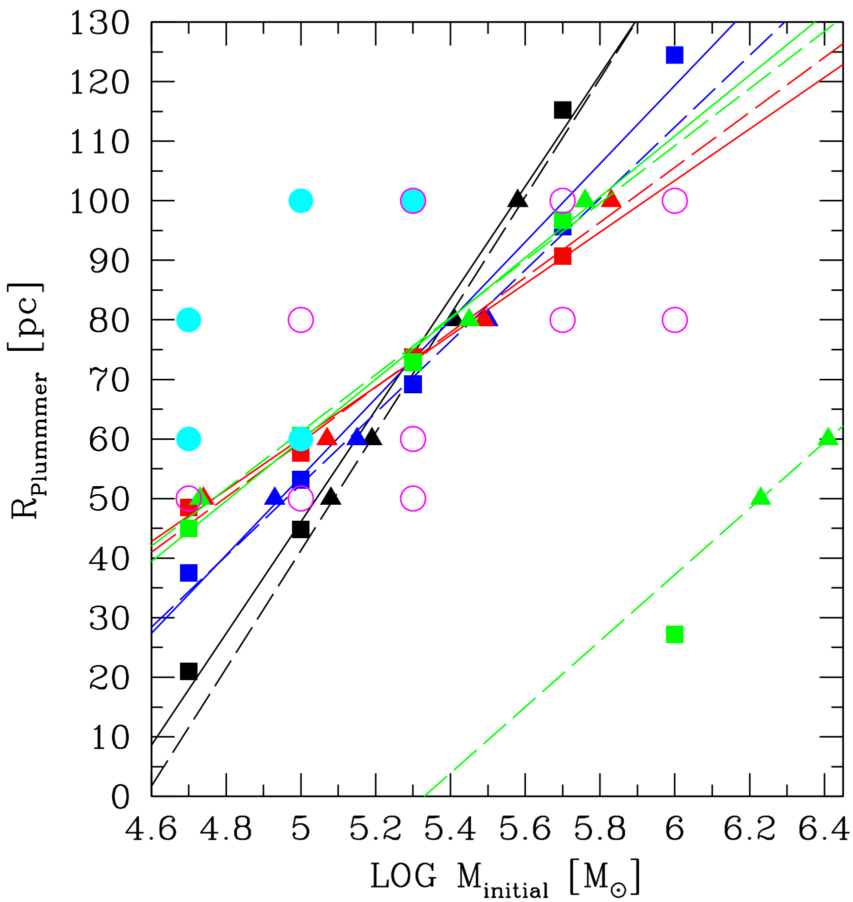

Figure 19: The parameter space of initial mass and Plummer radius. We show the extrapolated values which match the single observational facts and their corresponding fitting lines. The black symbols and line will show the fitting values of the final mass. The blue symbols and line represent the matching values of the central surface brightness. Red symbols and line match the effective radius of Hercules and finally green symbols and line are the matches for the velocity dispersion. The second green line in the lower right corner represents the bound regime with very massive solutions. The magenta circles show our matches of the angle of inclination and the cyan circles represent the simulations which approximately match the velocity gradient. We see that all lines intersect at the same point. This point is the unique solution for a Hercules model which is in the process of tidal destruction matching all the observables presented in this thesis.

6 Conclusions

We analyse several orbits for Hercules along its elongation, performing more than 600 simulations with the collisionless N-body code SUPERBOX (Fellhauer et al., 2000). We search through the initial parameter-space of mass and Plummer radius to find a plausible progenitor for Hercules. We then conduct an exhaustive analysis for the orbit proposed by Jin & Martin (2010) in our case A. This orbit is very eccentric, with a pericentre of $R_{\rm peri} = 5.7$ kpc which acts very destructively on the dwarf galaxy.

Our models constrain the solution area, of a 10 Gyr orbit, to a single and narrow area, with a range for Plummer radii between $\mathrm{R_{pl}} = 68$ pc and 80 pc, and a range for the initial total mass between: $\mathrm{M_{ini}} \approx 1.6\times10^5$ $\mathrm{M_\odot}$ and 2.5×10^5 $\mathrm{M_\odot}$. Having Hercules a luminous mass of $\approx 5 \times 10^4$ $\mathrm{M_\odot}$ implies a mass-loss of 70 % to 80 % of its luminous mass.

We must emphasize that our scenario does not consider dark matter. It is up to the reader to interpret this. We do not engage in any political or religious dispute whether or not dark matter exists. Only one thing we know for sure. If the elongation of Hercules is due to tidal distortion and therefore it is possible to determine its orbit (Jin & Martin, 2010), then it should be free of dark matter now. Simulations show that a galaxy harassed by tidal forces first looses up to 90 per cent of its dark matter before it starts to loose its stars. So our scenario starts either with the formation of a tidal dwarf galaxy on an orbit around the Milky Way or with a dark matter dominated dwarf which has already lost the majority of its DM, orbiting the MW. Our models also do not simulate gas, but just the dynamics of the stars.

We see in Fig. 19 that the matches for four of the observed properties: the final mass, surface-brightness, effective radius and velocity dispersion intersect at roughly the same point of initial parameter space. Even though our chosen initial model and infall time are arbitrarily, our models suggest that the uniqueness of the solution area will always be present (see the results in the Appendix for different infall times and different orbits).

The orientation along the orbit is difficult to match and we do not see general trend in form of power-laws. This is partly due to the fact that we do not measure these values at a certain physical extension but at a fixed extension matching the observations. But we do find matching solutions.

The mismatch in ellipticity can be cured by starting with flattened models.

The radial velocity gradient shows a trend with the initial mass, but it is scaterred and therefore we use values that match in a range around the observed value, which anyway fall between the observational errors.

Our models converge when Hercules is in the tidal regime, between the bound regime in virial equilibrium and the disrupted system in the unbound regime. The remaining mass and the mass-loss after each pass through the pericentre indicate that this would be the last passage of Hercules through pericentre before a total disruption.

In summary, for our choice of initial model (Plummer distribution) and our choice of Galactic potential (which is kept constant but is identical to the potential used to determine the orbit of Hercules) and our choice of simulation time (10 Gyr) we can find a unique initial model which matches the observations. We do not need any special conditions (peri- or apocentre) or a special time (exactly at the break-up), when we see the dwarf.

Once more, there *is* a model which matches Hercules and it contains no dark matter (it never had or at least it has lost its DM in the past). The elongation and velocity gradient of Hercules are indeed signs of tidal distortions and therefore mark its orbit.

References

Adén D., Eriksson K., Feltzing S., Grebel E.K., Koch A., Wilkinson M.I. 2011, A&A, 525, A153

Adén D., Wilkinson M.I., Read J.I., Feltzing S., Koch A., Gilmore G.F., Grebel E.K., & Lundtrm I. 2009, ApJ, 706, L150

Adén D., Feltzing S., Koch A., Wilkinson M.I., Grebel E.K., Lundtrm I., Gilmore G.F., Zucker D.B, Belokurov V., Evans N.W., and Faria D. 2009, A&A, 506, 1147

Belokurov V., et al. 2006, ApJ, 647, L111

Belokurov V., Zucker D.B., Evans N.W., Gilmore G., Vidrih S., Bramich D. M., Newberg H. J., Wyse R.F.G., Irwin M.J., Fellhauer, M., Hewett P.C., Walton N.A., Wilkinson M.I., Cole N., Yanny B., Rockosi C.M., Beers T.C., Bell E.F., Brinkmann J., Ivezi ., Lupton R. 2006, ApJ, 642, L137

Belokurov V., et al. 2007, ApJ, 654, 897

Binney J., & Tremaine S. (ed.) 2008, in Galactic Dynamics (2nd ed.; Princeton, NJ: Princeton Univ. Press)

Belokurov V., et al. 2008, ApJ, 686, L83

Boylan-Kolchin M., Springel V., White S.D., Jenkins A., Lemson G. 2009, MNRAS, 398, 1150

Coleman M.G., et al. 2007, ApJ, 668, L43

de Jong J.T.A., et al. 2008, ApJ, 680, 1112

de Jong J.T.A., Martin N.F., Rix H.-W., Smith K.W., Jin S., Macciò A.V. 2010, ApJ, 710, 1664

Diemand J., Kuhlen M., Madau P., Zemp M., Moore B., Potter D., Stadel J., 2008, Nature, 454, 735

Franois P., Monaco L., Villanova S., Catelan M., Bonifacio P., Bellazzini M., Moni Bidin C., Marconi G., Geisler D., Sbordone L., 2012, astro-ph, arXiv:1202.2899v2

Fellhauer M., Kroupa P., Baumgardt H., Bien R., Boily C., Spurzem R., Wassmer N. 2000, NewAst., Vol. 5, No. 6, 305

Fellhauer M., et al. 2006, MNRAS, 385, 1095

Fellhauer M., et al. 2007, MNRAS, 375, 1171

Fellhauer M., et al. 2008, MNRAS, 385, 1095

Grebel E., 2000, ESASP, 445, p.87

Geha M., Willman B., Simon J.D., Strigari L.E., Kirby E.N., Law D.R., Strader J. 2009, ApJ, 692, 1464

Ibata R. A., Gilmore G., & Irwin MM.J. 1995, MNRAS, 277,781

Illingworth G. 1976, ApJ, 204, 73

Irwin M.J., et al. 2007, ApJ, 656, L13

Irwin M.J., Hatzidimitriou D., 1995, MNRAS, 277, 1354

Irwin M.J., Bunclark P.S., Bridgeland M.T., & McMahon R.G. 1990, MNRAS, 244, 16P

Jin S., Martin N. 2010, ApJ, 721, L1333

Jin S., Martin N., de Jong J., Conn B., H.-W., Irwin M. 2012 to appear in the proceedings of the Subaru conference on Galactic Archaeology, Shuzenji, Japan (Nov. 1-4 2011), arXiv1201.5399

Kirby E., Simon J., Geha M., Guhathakurta P., Frebel A. 2008, ApJ, 685, L43

Klimentowski J., okas E., Kazantzidis S., Prada F., Mayer L. and Mamon G. 2007, MNRAS, 378, 353 - 368

Klimentowski J., okas E., Kazantzidis S., Mayer L., Mamon G., Prada F. 2009, MNRAS, 400, 4, 2162

Klypin A., Kravtsov A.V., Valanzuela O., Prada F. 1999, ApJ, 522, 82

Koch A., et al. 2009, ApJ, 690, 453

Koposov S., et al. 2008, ApJ, 686, 279

Kroupa P., Theis C., Boily C.M., 2005, A&A, 431, 517

Kroupa P., et al, 2010, A&A, 523, A32

Kuhlen M., Diemand J., Madau P., Zemp M. 2008, Journal of Physics: Conference Series, Vol. 125, Issue 1, p. 1

Lokas E.L., Mamon G.A. 2001, MNRAS, 321, 155

Macciò A.V., Dutton A.A., van den Bosch F.C. 2009, MNRAS, 391, 1940

Macciò A.V., Kang X., Fontanot F., Somerville R.S., Koposov S., Monaco P. 2010, MNRAS, 402, 1995

Martin N.F., de Jong J.T., & Rix H.-W. 2008, ApJ, 684, 1075

Merritt D., Graham A., Moore B., Diemand J., and Terzi B. 2006, AJ, 132, 2685M

Metz M., Kroupa P., Jerjen H. 2007, MNRAS, 374, 1125

Metz M., Kroupa P., Libeskind N.I. 2008, ApJ, 680, 287

Metz M., Kroupa P., Jerjen H. 2009, MNRAS, 394, 1529

Miyamoto M., Nagai R. 1975, PASJ, 27, 533

Moore B., Ghigna S., Governato F., Lake G., Quinn T., Stadel J., Tozzi P. 1999, ApJ, 524, L19

Moretti M.I., et al. 2009, ApJ, 699, L125

Muñoz R.R., Majewski S.J., Johnston K.V. 2008, ApJ, 679, 346

Navarro J.F., Frenk C.S., White S.D.M. 1997, ApJ, 490, 493

Paczyński B. 1990, ApJ, 348, 485

Pawlowski M.S., Kroupa P., de Boer K.S. 2011, A&A, 523, 118

Sawala T., Scannapieco C., White S. 2012, MNRAS, 420, 1714

Sand D.J., Olszewski E.W., Willman B., Zaritsky D., Seth A., Harris J., Piatek S., Saha A. 2009, ApJ, 704, 898

Sand D.J., Seth A., Olszewski E.W., Willman B., Zaritzky D., Kallivayalil N. 2010, ApJ, 718, 530

Simon J.D., Geha M. 2007, ApJ, 670, 313

Simon J.D., Frebel A., McWiliam A., Kirby E.N., Thompson I.B. 2010, ApJ, 716, 446

Spinnato P.F., Fellhauer M., Portegies Zwart S.F. (2003), MNRAS, 344, 22

Springel V., Wang J., Vogelsberger M., Ludlow A., Jenkins A., Helmi A., Navarro J.F., Frenk C.S. and White S.D.M. 2008, MNRAS, 391, 1685

Walker M.G., Belokurov V., Evans N.W., Irwin M.J., Mateo M., Olszewski E.W., Gilmore G. 2009, ApJ, 694, L144

Walker M.G., Mateo M., Olszewski E.W., Penarrubia J., Evans, N.W., Gilmore G. 2009, ApJ, 704, 1274

Walker M., Mateo M., Olszewski E., Gnedin O., Wang X., Sen B., Woodroofe M. 2007, ApJ, 667, L53

Walsh S.M., Jerjen H., Willman B. 2007, ApJ, 662, L83

Willman B., et al. 2005, ApJ, 626, L85

Wilkinson M.I., Kleyna J.T., Gilmore G.F., Evans N.W., Koch A., Grebel E.K., Wyse R.F.G., Harbeck D.R. 2006, Msngr, 124, 25

Xue X.X., et al 2008, ApJ, 704, 1274

York D.G., et al. 2000, AJ, 120, 1579Y

Zucker D.B., et al. 2006, ApJ, 643, L103

Zucker D.B., et al. 2006, ApJ, 650, L41

7 Appendix

7.1 Tables

Table 9: Results of Case B. The first column is the name of the simulation, the second corresponds to the initial total mass of the Plummer distribution. The third column is the Plummer radius. In the fourth and fifth columns we show the final bound mass M_{fin} and the final central surface-brightness respectively where we use a M^{stars}/ L_V=1 $\left[\frac{M_\odot}{L_\odot}\right]$. The sixth column is the final effective radius R_{eff} fitted with a Sersic-profile. The seventh column is the angle of inclination θ of the elongation respect to the axis of declination. The eight column is the final ellipticity of the dwarf galaxy. The ninth is the final central line-of-sight velocity dispersion and finally the last column corresponds to the final radial velocity gradient.

N°	M_{ini} [$M_\odot$]	R_{Plum} [pc]	M_{fin} [$M_\odot$]	μ_0 $\left[\frac{mag}{arcsec^2}\right]$	r_{ef} [pc]	θ [°]	ε	σ_{los} $\left[\frac{km}{s}\right]$	Δv_r $\left[\frac{km}{s\,deg/4}\right]$
			5.0E+4	27.2±0.6	230±30	-78	0.67	4	-7
1	1.0E+4	20	1.2E+3	28.6	95	-90	0.22	0.3	4
2	5.0E+4	20	2.9E+4	22.8	17	-90	0.01	0.7	-8.8
3	1.0E+5	20	7.2E+4	21.9	17	-78	0.02	0.9	-12
4	1.0E+4	30	0	32.8	1968	-80	0	1.5	24
5	5.0E+4	30	1.1E+4	25.9	35	-87	0.3	1	-4.4
6	1.0E+5	30	4.4E+4	23.9	28	-90	0.23	0.8	-7.2
7	1.0E+4	50	0	33.3	1408	-75	0.71	2	15
8	5.0E+4	50	0	32.3	1400	-82	0.33	3	23
9	1.0E+5	50	4.0E+3	29.7	204	0	0.70	1.8	4
10	5.0E+5	50	2.3E+5	23.5	45	-82	0	1.8	-4
11	1.0E+4	80	0	32.6	696	-78	0.7	2	-4
12	5.0E+4	80	0	32.9	4581	-78	0.07	5	-1.2
13	1.0E+5	80	0	31.8	994	-78	0.07	4	4.4
14	5.0E+5	80	3.5E+4	28.3	576	0	0.53	2	-7.6
15	1.0E+6	80	2.5E+5	24.7	88	-85	0.03	2	-6.8
16	1.0E+4	100	0	32.7	1666	-78	0.65	3	-3.2
17	5.0E+4	100	0	32.4	1580	-75	0.53	5	-4
18	1.0E+5	100	0	32.5	4998	0	0.53	6	-0.4
19	5.0E+5	100	0	31.8	1825	0	0.53	5	16
20	1.0E+6	100	7.0E+4	27.9	782	0	0.53	3	-8

Table 10: Results of Case C. The first column is the name of the simulation, the second corresponds to the initial total mass of the Plummer distribution. The third column is the Plummer radius. In the fourth and fifth columns we show the final bound mass M_{fin} and the final central surface-brightness respectively where we use a M^{stars}/ L_V=1 $\left[\frac{M_\odot}{L_\odot}\right]$. The sixth column is the final effective radius R_{eff} fitted with a Sersic-profile. The seventh column is the angle of inclination θ of the elongation respect to the axis of declination. The eight column is the final ellipticity of the dwarf galaxy. The ninth is the final central line-of-sight velocity dispersion and finally the last column corresponds to the final radial velocity gradient.

N^o	M_{ini} [$M_\odot$]	R_{Plum} [pc]	M_{fin} [$M_\odot$]	μ_0 $\left[\frac{mag}{arcsec^2}\right]$	r_{ef} [pc]	θ [^{o}]	ε	σ_{los} $\left[\frac{km}{s}\right]$	Δv_r $\left[\frac{km}{s\,deg/4}\right]$
			5.0E+4	27.2±0.6	230±30	-78	0	4	-7
1	1.0E+4	20	7.6E+3	24.3	16.4	-78	0	0.4	5.2
2	5.0E+4	20	4.7E+4	22.3	16.9	-78	0	0.8	-4
3	1.0E+5	20	9.7E+4	21.6	17.2	-80	0	1	0
4	1.0E+4	50	0	32.5	574.7	-78	0.7	0.4	7.6
5	5.0E+4	50	2.3E+4	25.4	43.4	-82	0.04	0.6	5.2
6	1.0E+5	50	6.6E+4	23.9	39.9	-90	0	0.8	-2.4
7	5.0E+5	50	4.6e+5	21.7	39.9	-90	0.05	1.2	0.4
8	1.0E+6	50	9.5e+5	20.9	40.3	-89	0.05	1.8	2.4
9	1.0E+4	100	0	33.0	1306	-78	0.61	0.7	8
10	5.0E+4	100	0	31.6	728	-78	0.5	0.7	4.8
11	1.0E+5	100	5.0e+3	29.7	296	5	0.49	0.5	1.6
12	5.0E+5	100	2.6e+5	24.1	85	-80	0	0.8	-4
13	1.0E+6	100	7.1e+5	22.8	78	-80	0	1.8	-1.2

7.2 Figures

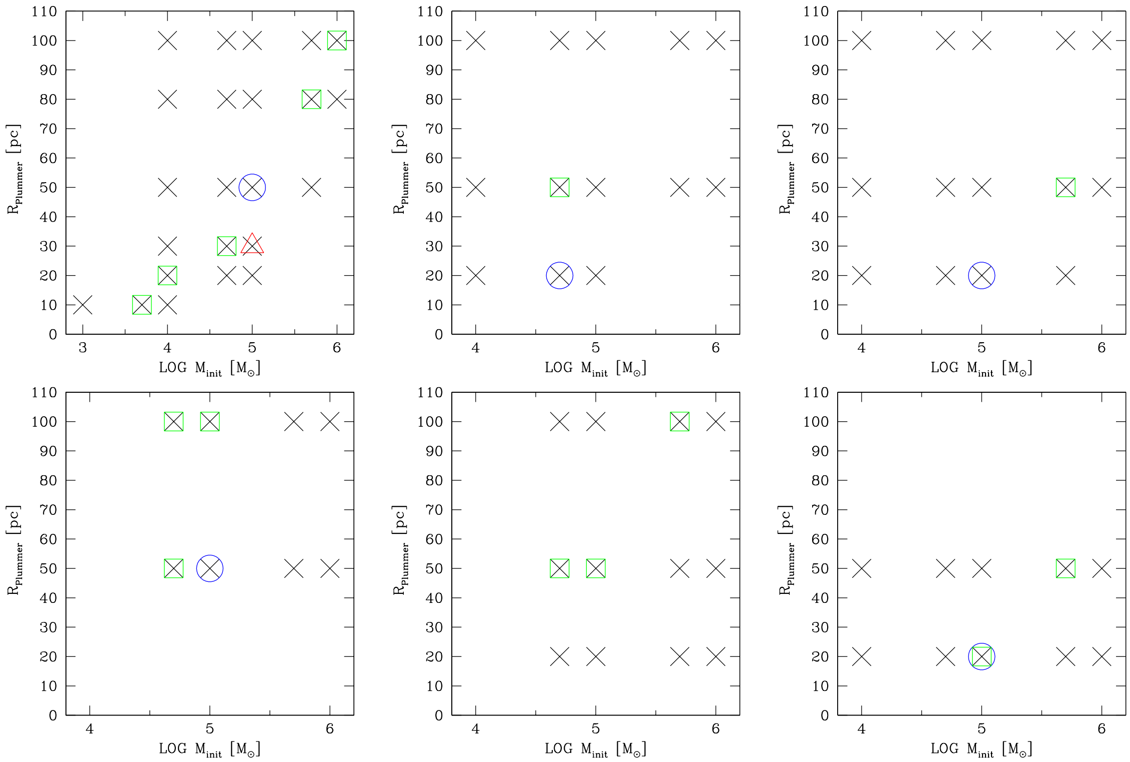

Figure 20: We plot the parameter space for the initial Plummer radius and the initial mass. We put an "$\times$" where we run simulations. The matches with the observations are represented in the plot as: final bound mass within a range of $\pm$ 20% (circles), the surface-brightness within a range of $\mu_o = 27 \pm 1$ [mag arcsec^{-2}] (squares) and the effective radius within (triangles). The panels are ordered as follow:: *Up-left*: case B, *up-centre*: case C, *up-right* case D, *down-left*: case E, *down-centre*: case F, *down-right*: case G.

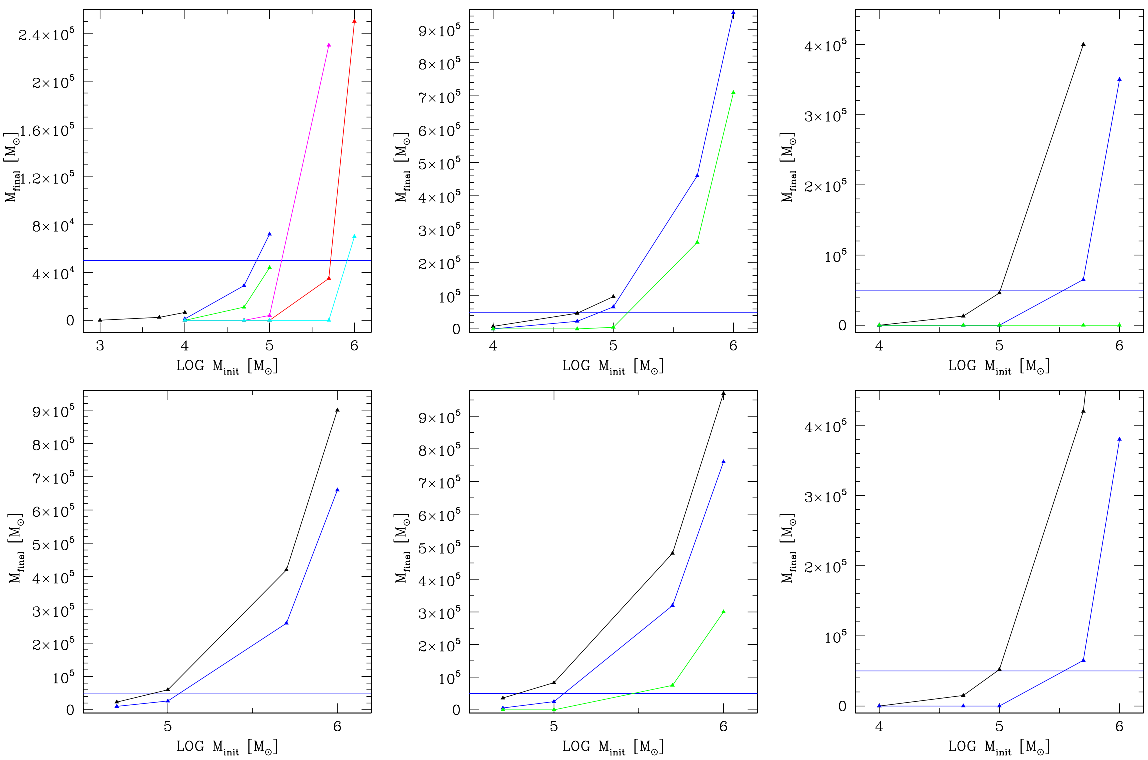

Figure 21: We plot the final mass (M_{fin}) versus the initial total mass (M_{init}), where each triangle corresponds to a simulation. The coloured lines indicate the Plummer radius. *Up-left*: case B black 10 pc, blue 20 pc, green 30 pc, magenta 50 pc, red 80 pc, cyan 100 pc; *up-centre*: case C black 20 pc, blue 50 pc, green 100 pc; *up-right*: case D black 20 pc, blue 50 pc, green 100 pc; *down-left*: case E black 50 pc, blue 100 pc; *down-centre*: case F black 20 pc, blue 50 pc, green 100 pc; *down-right*: case G black 20 pc, blue 50 pc.

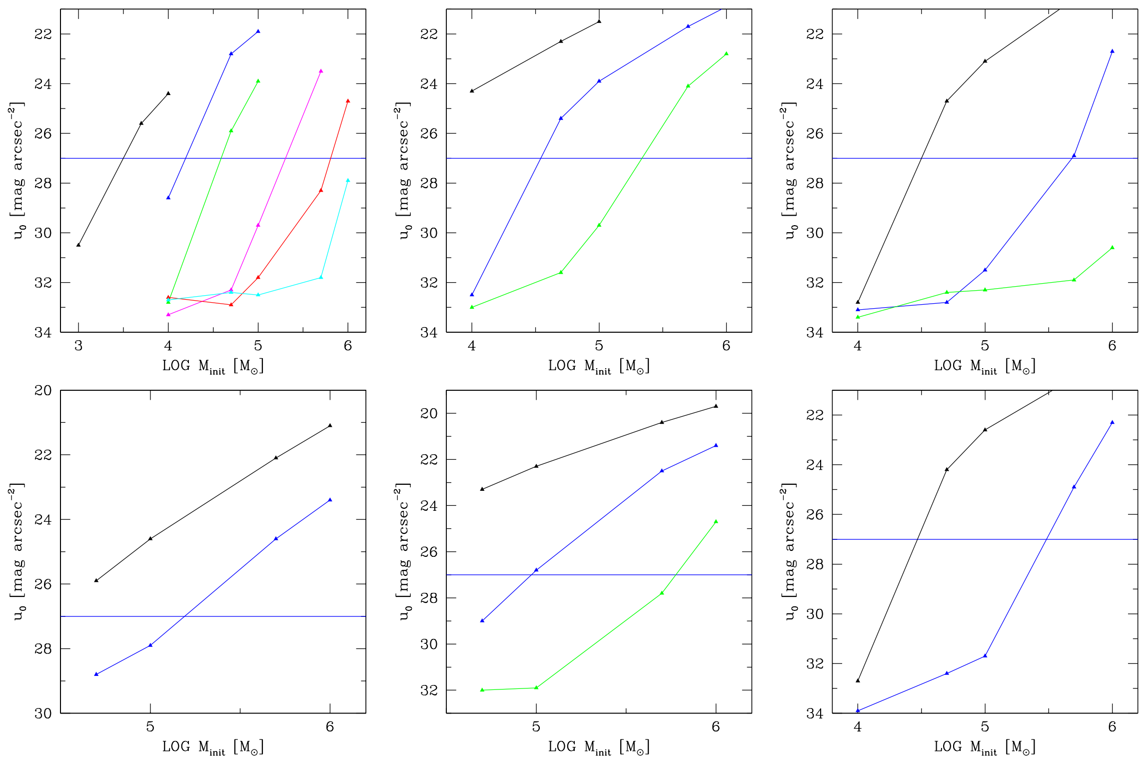

Figure 22: We plot the final central surface-brightness (μ_0) versus the initial total mass (M_{init}), where each triangle corresponds to a simulation. The coloured lines indicate the Plummer radius. *Up-left*: case B black 10 pc, blue 20 pc, green 30 pc, magenta 50 pc, red 80 pc, cyan 100 pc; *up-centre*: case C black 20 pc, blue 50 pc, green 100 pc; *up-right*: case D black 20 pc, blue 50 pc, green 100 pc; *down-left*: case E black 50 pc, blue 100 pc; *down-centre*: case F black 20 pc, blue 50 pc, green 100 pc; *down-right*: case G black 20 pc, blue 50 pc.

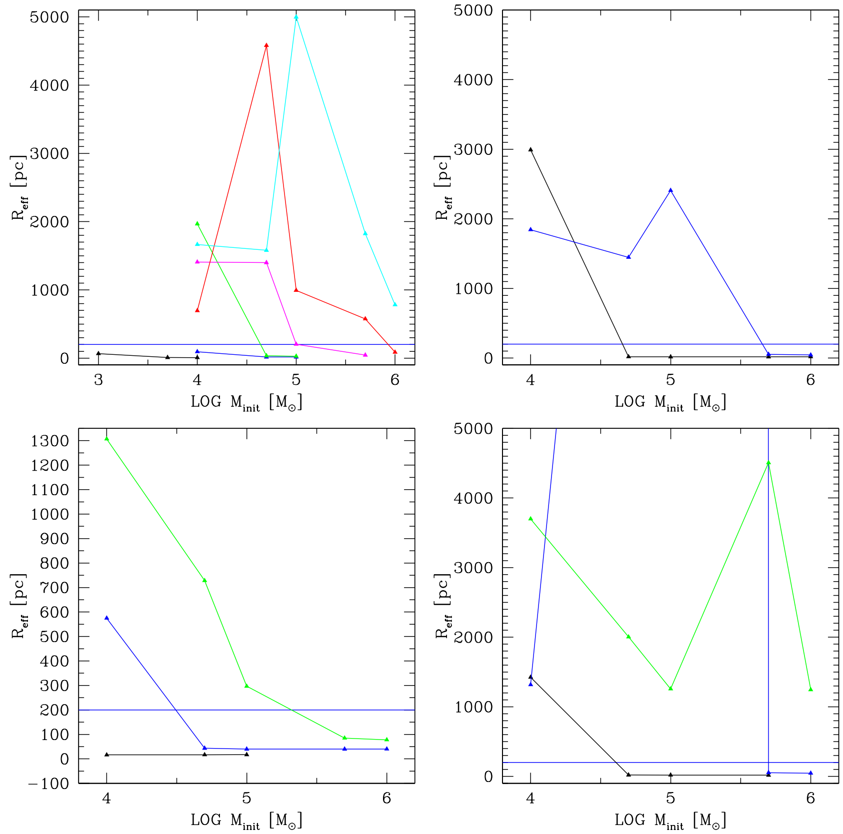

Figure 23: Here we plot the effective radius (R_{eff}) versus the initial total mass (M_{init}) for cases with the same infall time (10 Gyrs), where each triangle corresponds to a simulation. The coloured lines indicate the Plummer radius. *Up-left*: case B black 10 pc, blue 20 pc, green 30 pc, magenta 50 pc, red 80 pc, cyan 100 pc; *up-right*: case G black 20 pc, blue 50 pc; *down-left*: case C black 20 pc, blue 50 pc, green 100 pc; *down-right*: case D black 20 pc, blue 50 pc, green 100 pc.

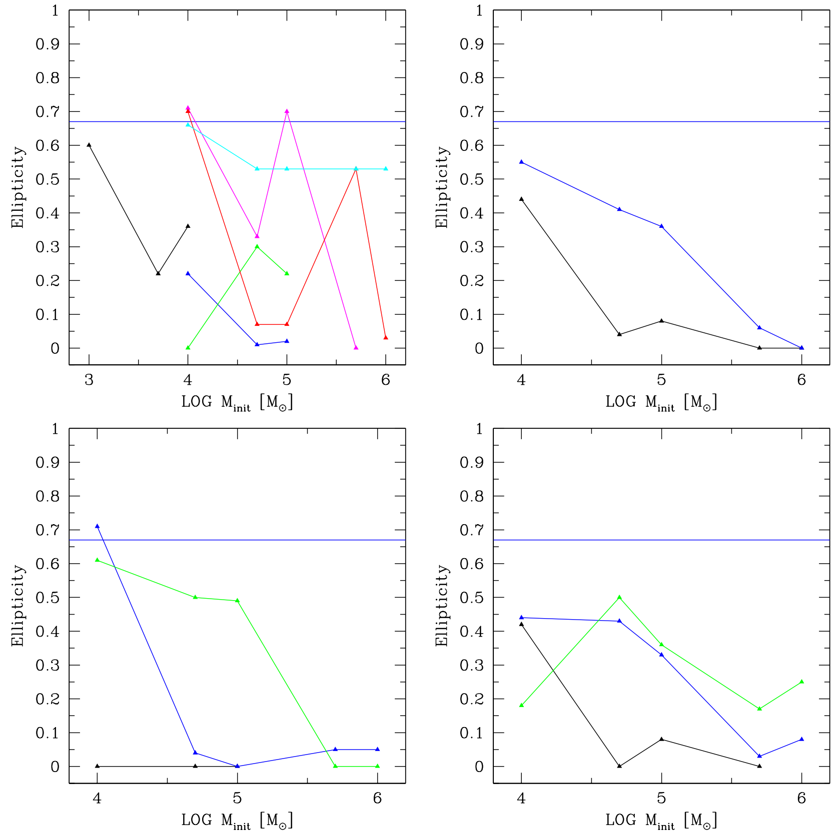

Figure 24: Here we show the ellipticity (ε) for cases with the same infall time (10 Gyrs). *Up-left*: case B black 10 pc, blue 20 pc, green 30 pc, magenta 50 pc, red 80 pc, cyan 100 pc; *up-right*: case G black 20 pc, blue 50 pc; *down-left*: case C black 20 pc, blue 50 pc, green 100 pc; *down-right*: case D black 20 pc, blue 50 pc, green 100 pc.

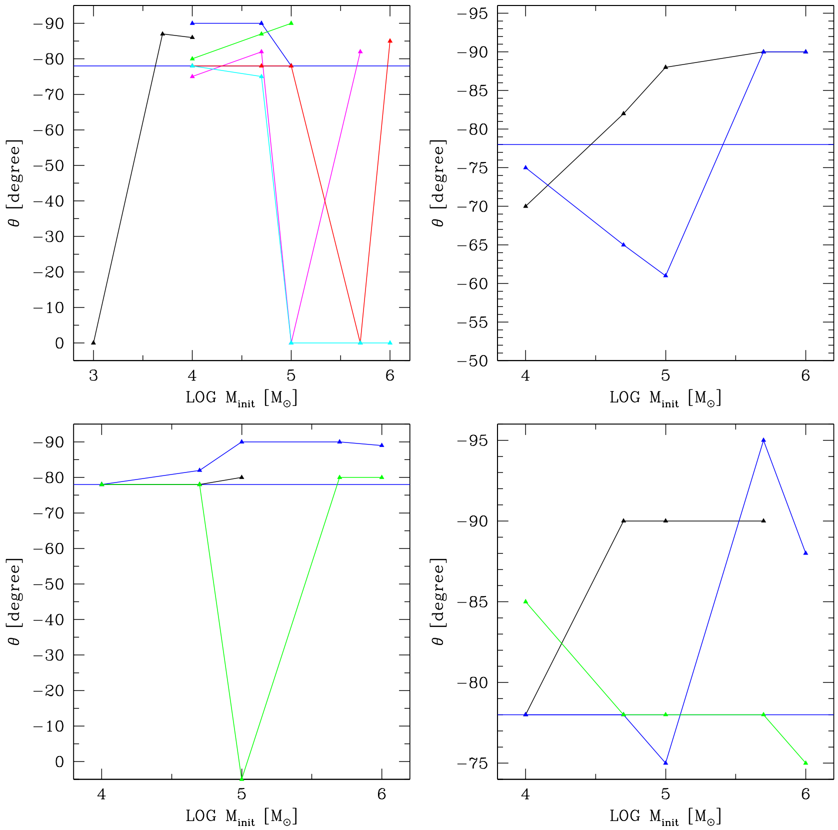

Figure 25: Here we show the angle of inclination (θ) for cases with the same infall time (10 Gyrs). *Up-left*: case B black 10 pc, blue 20 pc, green 30 pc, magenta 50 pc, red 80 pc, cyan 100 pc; *up-right*: case G black 20 pc, blue 50 pc; *down-left*: case C black 20 pc, blue 50 pc, green 100 pc; *down-right*: case D black 20 pc, blue 50 pc, green 100 pc.

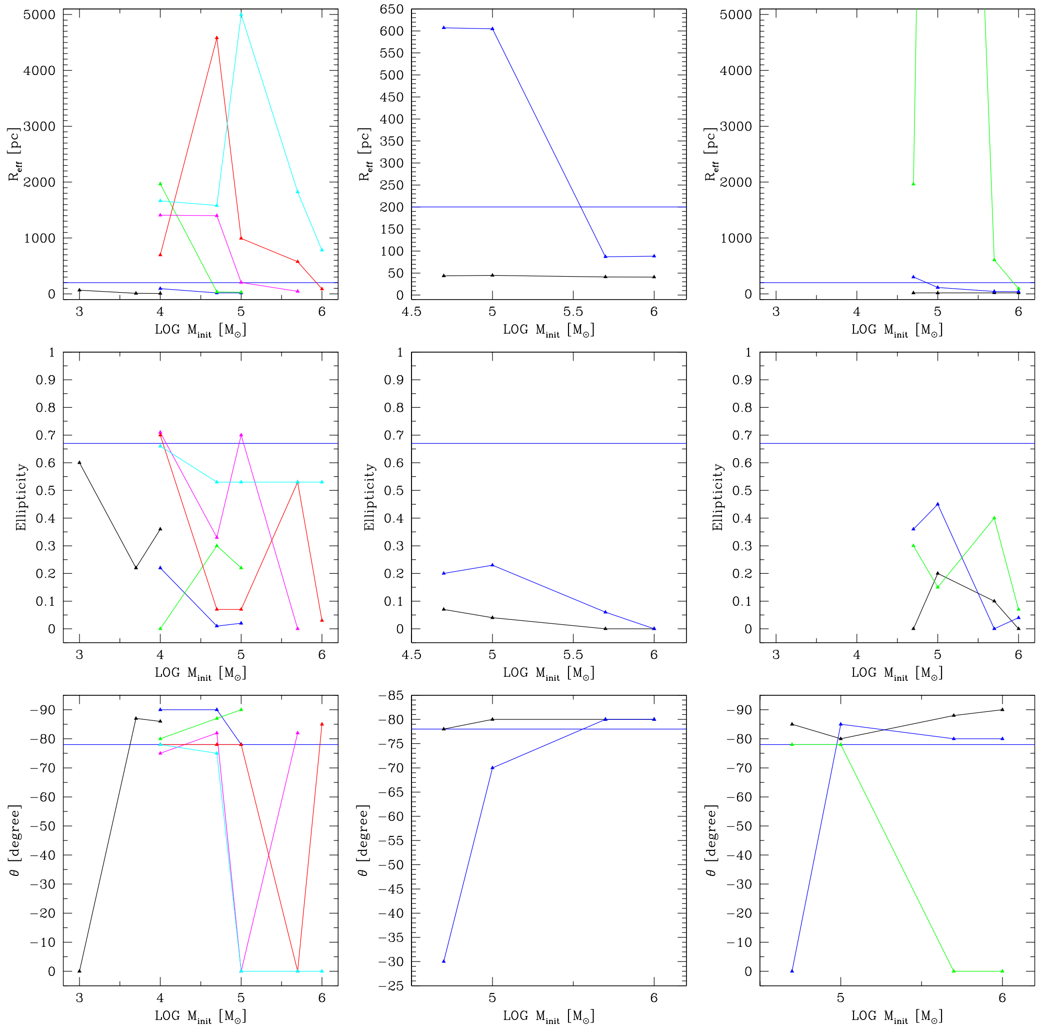

Figure 26: Here we compare cases with the same infall time (10 Gyrs), where each triangle corresponds to a simulation. The 3 panels at the left column correspond to case B where the colors indicate the Plummer radii: black 10 pc, blue 20 pc, green 30 pc, magenta 50 pc, red 80 pc, cyan 100 pc; the 3 panels in the middle column corresponds to case E where the colors indicate the Plummer radii: black 50 pc, blue 100 pc; and the 3 panels at the right column correspond to case F where the colors indicate the Plummer radii: black 20 pc, blue 50 pc, green 100 pc; The upper, middle and down lines of panles corresponds respectively to the final effective radius $R_{\rm eff}$, ellipticity and angle of inclination θ versus the logarithm of the initial total mass $M_{\rm init}$.

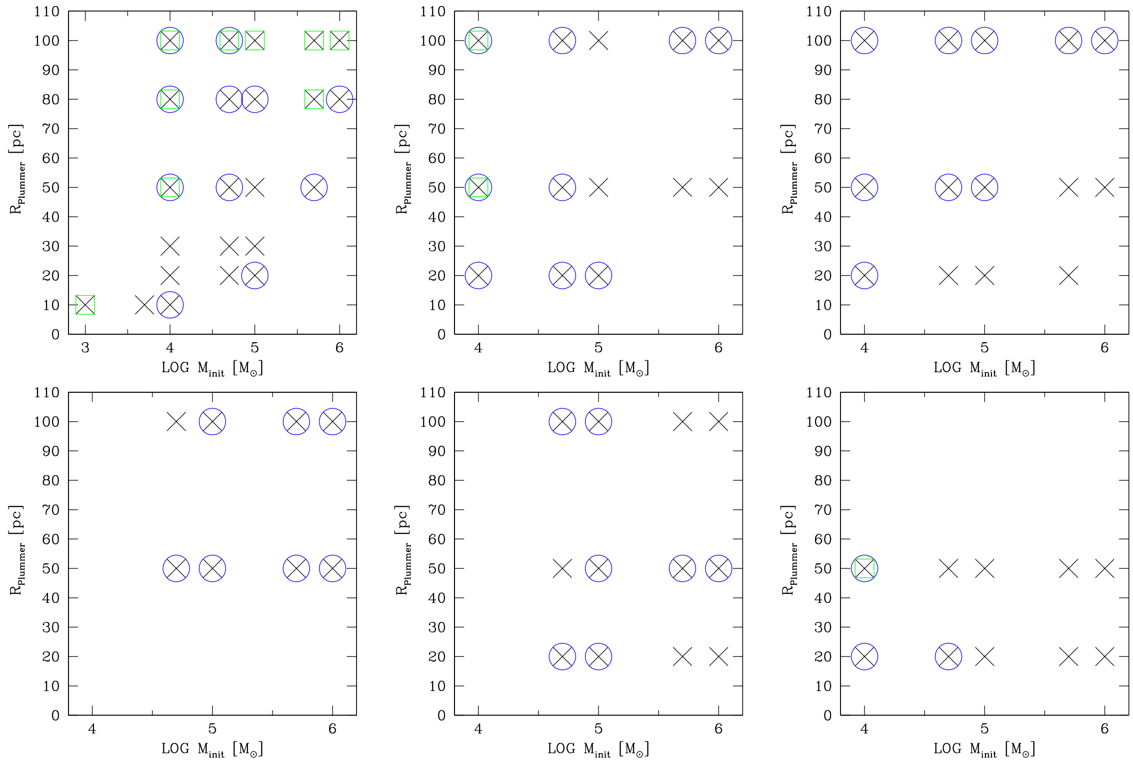

Figure 27: We plot the parameter space for the initial Plummer radius and the initial mass. We put an "$\times$" where we run simulations. The matches with the observations are represented in the plot as: final angle of inclination within a range of $\pm$ 10% (circles) and the ellipticity within a range of $\pm$ 20% (squares). Angle of inclination theta and ellipticity. *Up-left*: case B, *up-centre*: case C, *up-right*: case D, *bottom-left*: case E, *bottom-centre*: case F, *bottom-right*: case G.

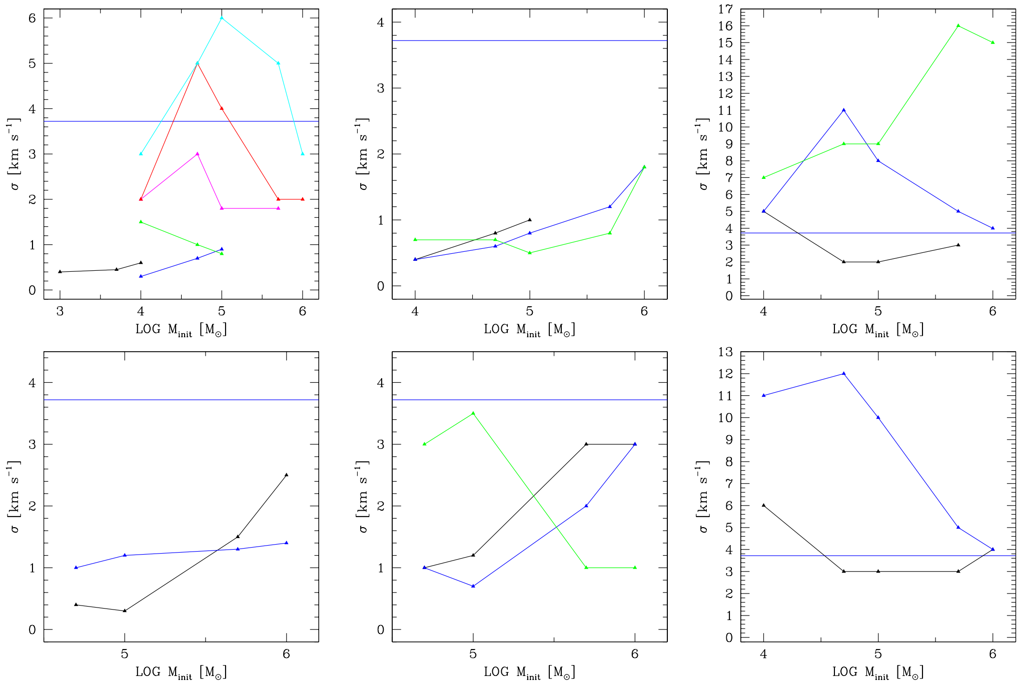

Figure 28: Velocity dispersion for cases: *Up-left*: case B black 10 pc, blue 20 pc, green 30 pc, magenta 50 pc, red 80 pc, cyan 100 pc; *up-centre*: case C black 20 pc, blue 50 pc, green 100 pc; *up-right*: case D black 20 pc, blue 50 pc, green 100 pc. *bottom-left*: case E black 50 pc, blue 100 pc; *bottom-centre*: case F black 20 pc, blue 50 pc, green 100 pc; *bottom-right*: case G black 20 pc, blue 50 pc;

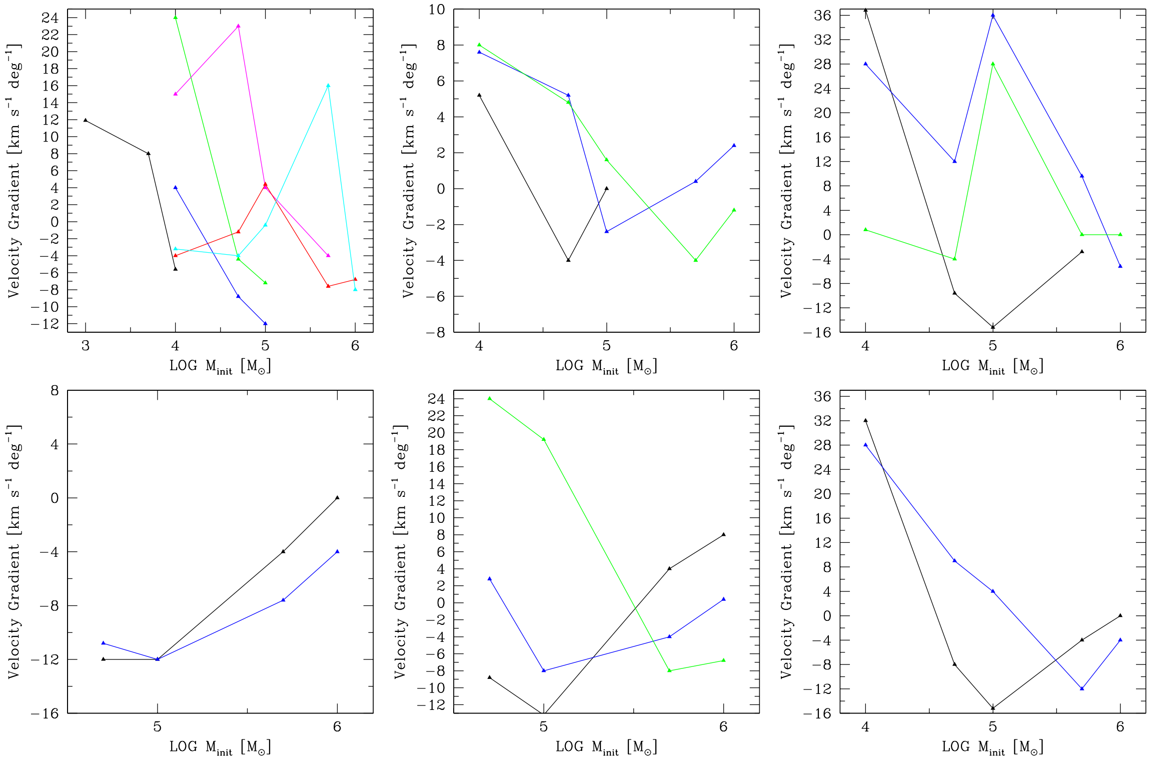

Figure 29: Velocity gradient for cases: *Up-left*: case B black 10 pc, blue 20 pc, green 30 pc, magenta 50 pc, red 80 pc, cyan 100 pc; *up-centre*: case C black 20 pc, blue 50 pc, green 100 pc; *up-right*: case D black 20 pc, blue 50 pc, green 100 pc. *bottom-left*: case E black 50 pc, blue 100 pc; *bottom-centre*: case F black 20 pc, blue 50 pc, green 100 pc; *bottom-right*: case G black 20 pc, blue 50 pc;

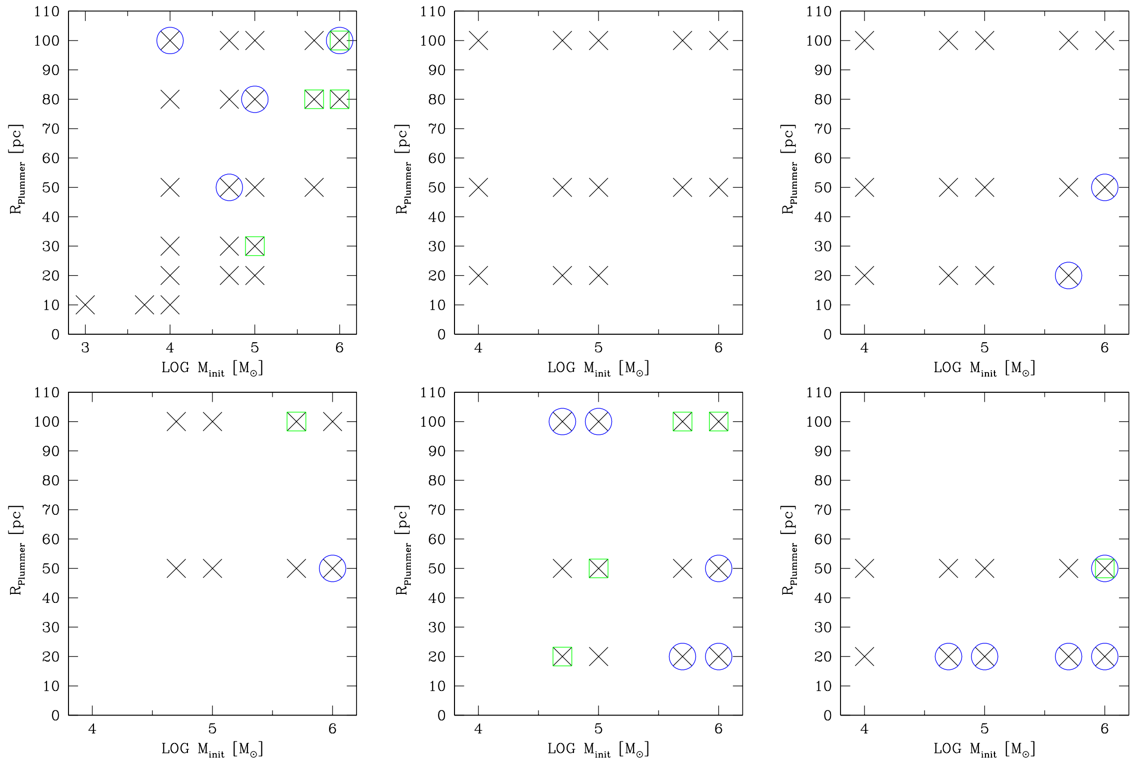

Figure 30: Velocity dispersion and velocity gradient for cases: *Up-left*: case B, *up-centre*: case C, *up-right*: case D, *bottom-left*: case E, *bottom-centre*: case F, *bottom-right*: case G.

8 Acknowledgments

Mediante esta tesis concluyo esta importante etapa de mi vida, pero no lo hago solo pues numerosas personas estuvieron involucradas en mi formación profesional y por sobre todo personal. Es la punta de un iceberg de bastantes años de inolvidables y olvidables experiencias. Mi elección de la Ciencia como centro de mi atención profesional trasciende hacia el plano personal, hacia un plano filosófico de índole metafísico. Y la Astronomía con su cosmovisión macroscópica, empírica y teórica me entrega precísamente eso, y agradezco profundamente a todas las personas que contribuyeron para que pudiera seguir este camino.

Y todo esto no hubiera sido posible de no ser por personas como mis amados padres, *Claudio Blaña de la Cruz* y *Ana Díaz Aliste*, quienes con su apoyo constante e incondicional me ayudaron a seguir este hermoso camino. Les estaré agradecido hasta la eternidad por todos sus años de esfuerzo. También agradezco de profundo corazón a mis hermanos que son casi mis segundos padres, *Claudio Blaña Díaz* y *Heidi Blaña Díaz*, por su constante apoyo. Extiendo también mis agradecimientos a toda mi familia, a mis abuelas Omi, la Abue y abuelos, tios, primos, cuñados y sobrinos por esos momentos felices.

También agradezco a la *Burschenschaft Montania* y a todos sus miembros por todos estos años de grandiosas experiencias y recuerdos. Dichas experiencias me entregaron la comprensión de la importancia de los ideales como guías: *Ehre, Freundschaft und Recht* y de lo difícil que es plasmarlas y mantenerlas en la *realidad*: *"Die Ideale sind ein Leuchtturm, kein Hafen"*. Por ello agradezo profundamente a mis *Bundesbrüder*: *Schiffer, Allenthao, Jako, Droopy, Manta, Zerstörer, Wethy Wop, Schokolade, Skatmann, Bisbald, Kayeukhe, Leeche, Nachteule, Sechsa Piehl, Dihazepahm, Leopard, Galgho, Zombie, Neohpren, Malignuss, Malditus, Parvulito, Simon, Frosch, Lavin, Osram y muchos más.*

También agradezco a todos eso amigos que la vida (y el terremoto) me trajo, *Robert, Nestor, Urzula, Annette, Ciro, Rhodia, Gustavo* y muchos más, junto a los cuales tuve interesantes conversaciones como con el grupo de los *Cangrejos*.

Agradezo a mis profesores del colegio, en especial al *Profesor Luis González*, por todas esas charlas sobre física en los recreos, que reforzaron mi interés por la Ciencia.

También agradezco a la *Universidad de Concepción* y a toda la gente que ahí trabaja. El carácter laico, académico y de vocación social de esta universidad ayudaron a forjarme un espírutu con dichos atributos. Y a la gente que conocí en esta etapa les doy las gracias; a mis compañeros de universidad y amigos astronómico que conocí en conferencias, por todos esas noches de estudio y festejos, tanto de la vieja carrera de CFA como de la nueva carrera de Astronomía: *Mairon, Pamela, Coté, Roy, Fabián, Fede, Gustavo O., Gustavo A., Bego, Carolina S., Leonardo, Carolina A., Daniela, Rodrigo, Mónica, Caddy y César* entre otros. Agradezco al Departamento de Física, donde se formaron mis bases académicas.y a sus profesores *Dr. Jaime Araneda, Dr. Claudio Faúndez, Dr. Joaquín Díaz de Valdéz, Dr.*

Paulraj Manidurai, Dr. Guillermo Rubilar, Dr. Patricio Salgado, Dr. Rolando Hernández y a muchos más.
Y al Departamento de Astronomía y a los profesores de mi comisión; al *Dr. Ricardo Demarco* por siempre compartir su entusiasmo y conocimientos científicos, y muy especialmente al *Dr. Neil Nagar* por todos esos años de clases que siempre ha realizado mostrando gran simpatía y un gigantezco compromiso con sus estudiantes, les estaré siempre agradecidos. Y agradezco también a la señora *Jeanette Espinoza*, a don *Victor Mora* y en especial a la señora *Marcela Sanhueza* por cuidarnos maternalmente todos estos años de pregrado, defendiendonos de la burocracia, y a *Ronald Burgos* por salvar a mi computador tantas veces. Agradezco también a los doctorandos y postdoctorados, *Richard Lane*, *André-Nicolas Chené*, *Roger Leiton*, *Ricardo Bustos*, *Renee Mateluna*, *Francesco Mauro*, *Bogumil Pilecki*, *Hugo Messias* y *Paulina Assmann* por el conocimiento tanto científico como de la vida del científico que compartieron conmigo. Le extiendo un especial agradecimiento al grupo de teoría por sus aportes en mi formación científica: Al *Dr. Rory Smith* por todas esas discusiones interesantes y su gran apoyo para realizar posters y charlas en conferencias. Estoy seguro que los nuevos integrantes del grupo, *Juan Pablo Farías* y el *Dr. Graeme Candlish* aprenderán y aportarán mucho al grupo. Y muy especialmente agradezco al Profesor *Dr. Michael Fellhauer*, por confiar y potenciar mis habilidades y por su gran compromiso como profesor supervisor, permitiéndome desde el comienzo realizar interesantes proyectos de investigación que concluyeron con publicaciones en revistas reconocidas. Y por apoyar e incentivar mi participación en conferencias nacionales e internacionales y en general por darle un gran empuje a mi carrera profesional, le estaré eternamente muy agradecido.

Mas el pasado y el presente se reúnen en este trabajo para mirar hacia un futuro de posibilidades. Un ciclo ha concluido, pero muchos más habrán de venir.

A todos les doy mis más sinceros agradecimientos,

Matías Andrés Blaña Díaz